Crustal Anisotropy from the Birefringence of P-to-S Converted Waves: Bias Associated with P-Wave Anisotropy

Jeffrey Park^{1,*}, Xiaoran Chen² and Vadim Levin²

- (1) Department of Earth and Planetary Sciences, Yale University, New Haven CT, USA
- (2) Department of Earth and Planetary Sciences, Rutgers University, Piscataway NJ, USA

Article history: received July 22, 2022; accepted March 30, 2023

Abstract

Many researchers have used the birefringence of P-to-S converted waves from the Moho discontinuity to constrain the anisotropy of Earth's crust. However, this practice ignores the substantial influence that anisotropy has on the initial amplitude of the converted wave, which adds to the splitting acquired during its propagation from Moho to the seismometer. We find that large variations in Ps birefringence estimates with back-azimuth occur theoretically in the presence of P-wave anisotropy, which normally accompanies S-wave anisotropy. The variations are largest for crustal anisotropy with a tilted axis of symmetry, a geometry that is often neglected in birefringence interpretations, but is commonly found in Earth's crust. We simulated globally-distributed P-coda datasets for 36 distinct 4-layer crustal models with combinations of elliptical shear anisotropy or compressional anisotropy, and also incorporated the higher-order anisotropic Backus parameter C. We tested both horizontal and tilted symmetry-axis geometries and tested the birefringence tradeoff associated with Ps converted phases at the top and bottom of a thin high- or low-velocity basal layer. We computed composite receiver functions (RFs) with harmonic regression over back azimuth, using multipletaper correlation with moveout corrections for the epicentral distances of 471 events, to simulate a realistic data set. We estimate Ps birefringence from the radial and transverse RFs, a strategy that is similar to previous studies. We find that Ps splitting can be a useful indicator of bulk crustal anisotropy only under restricted circumstance, either in media with no compressional anisotropy, or if the symmetry axis is horizontal throughout. In other, more-realistic cases, the inferred fast polarization of Ps birefringence estimated from synthetic RFs tends either to drift with back-azimuth, form weak penalty-function minima, or return splitting times that depend on the thickness of an anisotropic layer, rather than the birefringence accumulated within it.

Keywords: Seismic anisotropy; Receiver functions; Shear-wave splitting; Crustal structure; Moho discontinuity

1. Introduction

When the birefringence of core-refracted shear waves [Vinnik et al., 1986; Silver and Chan, 1991], also known as SKS splitting, was first applied to broadband seismic data in the Basin and Range Province [McNamara and Owens, 1993] and central Tibet [McNamara et al., 1994] to explore deformation in the underlying mantle, the bias associated with crustal anisotropy was constrained by the birefringence of Moho-converted Ps waves. Though smaller than mantle-induced splitting ($\delta t \sim 0.2$ -0.4 sec for Ps, compared with $\delta t \sim 1$ -2 sec for SKS) typical Ps-splitting times were consistent with 2% crustal-average azimuthal anisotropy or more. Barruol and Mainprice [1993] argued that typical continental lithologies were consistent with 0.1-0.2 s splitting delays per 10 km of crustal thickness, agreeing with these observations. Subsequently, many studies have interpreted Ps birefringence in terms of crustal deformation [Nagaya et al., 2011; Chen et al., 2013; Kong et al., 2016; Xu et al., 2018]. At the same time, other studies have focused on the effects of anisotropy on the amplitude of the Ps converted phase [Levin and Park, 1998; Eckhardt and Rabbel, 2011; Wirth and Long, 2012; Schulte-Pelkum and Mahan, 2014; Park and Levin, 2016al, and interpreted harmonic variation in the radial and transverse receiver functions (RFs) of selected stations in terms of anisotropy with either a horizontal or tilted symmetry axis [Levin and Park, 1998; Levin et al, 2002; Liu et al., 2015; Olugboji and Park, 2016; Xie et al., 2020; Li et al., 2021, Chen et al., 2021a]. Finally, a dipping Moho can also cause harmonic variation in Ps amplitude with event back azimuth ξ [Savage, 1998; Lucente et al., 2005; Park and Levin, 2016a]. A dipping interface may be distinguishable from anisotropy via Ps delay-time moveout from updip to downdip back azimuths [Park et al., 2004; Shiomi and Park, 2008].

Liu and Park [2017] compared the effects of Ps amplitude variation associated with a thin anisotropic layer at the base of the crust and Ps birefringence. These two effects contribute similarly to Ps RFs, with the Ps conversions at the top and bottom of a basal anisotropic layer mimicking the fast and slow split Ps waves in a crust that is anisotropic from surface to Moho. For three long-running stations of the Global Seismographic Network [Butler et al., 2004], Liu and Park [2017] argued that thin layers of strong anisotropy explained the RFs better than Ps birefringence. However, simple criteria for choosing one interpretation over the other are still lacking, especially as physics predicts that both effects should contribute to the seismogram to some extent.

In this contribution for the special issue in Annals of Geophysics on shear-wave splitting, we focus on the anisotropic parameters and wave-propagation effects that help distinguish Ps amplitude variations from thin anisotropic layers and Ps splitting that accumulates throughout the crust, extending the data-synthetics comparisons of Liu and Park [2017]. Rather than analyze individual event synthetics for Ps birefringence, we show that the standard minimum-transverse method for estimating shear-wave splitting can be applied to the radial and transverse receiver functions. The RFs combine information for many seismograms to estimate the response of a layered medium to a pulse-like input. We find that simple crustal models that include only shear anisotropy are estimated well by RF birefringence. However, the Ps amplitude variation induced by compressional anisotropy leads to misleading estimates of birefringence.

For this study, we computed synthetic seismograms for a total of 36 anisotropic crustal models, to examine the effects on Ps birefringence of shear (S) or compressional (P) anisotropy, tilted or horizontal anisotropic fabric, and the depth range of anisotropy. We present the back-azimuth dependence of receiver functions and their harmonic dependence for all 36 models in the Online Supplement. In the main body of this paper we discuss in more detail a smaller collection of the studied models, in order to generalize the merits and pitfalls of Ps birefringence estimation.

In Section 2, we define anisotropic parameters, seismogram synthesis, and RF analysis. Section 3 examines the best cases for reliable interpretations of Ps splitting: pure shear anisotropy with a horizontal axis of symmetry. Section 4 examines Ps splitting in the context of realistic anisotropy, with compressional anisotropy or tilted-axis geometry. Section 5 examines the oft-neglected influence of the Backus parameter C, a higher-order harmonic term for compressional anisotropy. Section 6 examines the problematic case where a thin anisotropic layer at the base of the crust is interpreted with Ps splitting. Section 7 estimates Ps splitting in real data from three long-running seismological observatories, which illustrates some of the behaviors found in synthetic seismograms in anisotropic media.

2. Methods

Although general anisotropy depends on 21 independent components of the elastic tensor, and synthetic seismogram codes for the general tensor are available [Tesoniero et al., 2020; Chen et al., 2021b], seismic data are typically interpreted in terms of anisotropy with a symmetry axis that is either vertical, horizontal or tilted. Seven independent parameters describe such a model. The first two are the strike θ (cw from N) and tilt ψ (down from the vertical) of the symmetry axis \hat{w} . The remaining five parameters specify a low-order harmonic expansion of squared seismic wavespeed that depends on the angle ζ between the symmetry axis \hat{w} and the wavenumber vector \hat{k} of a plane wave propagating in the anisotropic medium [Backus, 1965]:

$$\rho\alpha^{2} = A + B\cos 2\zeta + C\cos 4\zeta$$
$$\rho(\beta_{SV})^{2} = D + E\cos 2\zeta$$

In this expansion α is the compressional (P) wavespeed and β is a shear (S) wavespeed with polarization \hat{s} that is normal to both \hat{w} and \hat{k} . In the standard geometry for head waves in marine refraction, with both \hat{w} and \hat{k} horizontal, \hat{s} aligns with the vertical and is the SV polarization. The quantities $\rho\alpha^2$ and $\rho\beta^2$ have traction units, i.e., force/area, so that the Backus parameters A, B, C, D, and E populate the elastic tensor in various linear combinations with coefficients that involve the strike θ and tilt ψ of the symmetry axis \hat{w} . To first order, the ratio B/A is the peak-to-peak relative variation of P wavespeed α specified by $\cos 2\zeta$ dependence on the propagation angle ζ relative to the fast axis. Also to first order, the ratio E/D is the peak-to-peak relative variation of S wavespeed β for the polarization \hat{s} . The shear-wavespeed for the second shear polarization (SH in the marine-refraction scenario) includes a $\cos 4\zeta$ term that depends linearly on C [Park, 1996]:

$$\rho(\beta_{SH})^2 = D + E + C (1 - \cos 4\zeta).$$

This wavespeed variation is not typically observed in active-source seismology, because SH waves are not directly excited with explosive sources.

Although attempts to constrain the parameter C in the Backus [1965] formulation predate the plate-tectonics paradigm in marine refraction [Raitt et al., 1969] and recent mineral-physics work highlights how C values help distinguish crustal mineralogy [Brownlee et al., 2017], most geologic interpretations of seismic data involve the lower-order "elliptical" parameters B and E. The polarity of these parameters defines fast (B,E>0) and slow (B,E<0) symmetry axes in which extremal wavespeeds occur for plane waves that propagate parallel to the symmetry axis \hat{w} , balanced by oppositely perturbed wavespeeds in a girdle of wave-propagation directions normal to \hat{w} [Maupin and Park, 2015]. Brownlee et al. [2017] argue from a collection of elastic tensors for minerals and rocks that C scales linearly with B, with independent proportion constants for mica-rich and amphibole-rich rock types. We adopt the mica-rich scaling for the Backus parameter C in this paper, which Brownlee et al. [2017] found consistent with most crustal rocks that possess a slow axis of symmetry. Amphibole-rich rocks are thought to be more abundant in the lower crust, but for this study we omit this modelling feature.

We compute synthetic seismograms with the reflectivity algorithm in one-dimensional anisotropic earth models comprised of a finite number of horizontal layers above a halfspace, each with constant properties [Chen, 1993; Park, 1996; Levin and Park, 1997; Chen et al., 2021b]. Perturbation theory [Park and Levin, 2016a] argues that Ps and Sp waves arise at sharp interfaces, to first order, from the hybridization of P and S waves in anisotropic media. In addition to the isotropic P-to-SV converted phase, Ps scattered waves with both SV and SH polarization arise at both the top and bottom of an anisotropic layer to cancel the secondary shear component of the P wave. Similarly, Sp scattered waves arise to cancel the secondary compressional component of the S wave at the same anisotropic interfaces.

We estimate receiver functions (RFs) from synthetic and real data by means of multiple-taper spectral correlation [Park and Levin, 2000; Park and Levin, 2016b], using harmonic regression over back azimuth ξ [Bianchi et al., 2010; Liu et al, 2015; Park and Levin, 2016a; Xie et al., 2020] to detect anisotropic effects. The radial and transverse RFs

in a layered anisotropic structure show a predictable phasing relationship with back azimuth ξ that can be stacked for [Schulte-Pelkum and Mahan, 2014]. Beyond simple stacking, this radial-transverse combination can define harmonic-regression terms for a least-squares fit over back azimuth ξ [Park and Levin, 2016a]. The researcher can validate the anisotropic or dipping-interface assumption by checking that the RF regression terms with the "unmodelled" radial-transverse RF combinations have small amplitude relative to the RF combinations predicted by simple 1-D theory, see Li et al. [2021] and Chen et al. [2021a].

Receiver functions comprise estimates of how incoming seismic waves scatter and propagate upward through a 1-D structure beneath a seismic receiver, deconvolving the earthquake rupture into a simple pulse, in theory. The Ps converted wave in a receiver function is also a simple pulse on the radial-component RF only, with a time delay, if the structure has 1-D isotropic layering. If the crust is anisotropic, the Ps converted wave may suffer birefringence, so that the radial and transverse RFs describe elliptical motion, similar to that exhibited by core-refracted SV waves [Silver and Chan, 1991]. When birefringence is estimated from shear waves from single events at a single station, one typically lowpasses the data to simplify the body-wave pulse, and often classifies a large proportion of a dataset as "null" splitting [Wüstefeld et al., 2008]. RF estimates, at least for Ps splitting, offer the possibility to deconvolve complex body wave pulses and combine multiple observations to increase signal over noise.

We explored a family of anisotropic distributions and geometries with a simple four-layer model above an isotropic halfspace (Figure 1). Models were defined with constant anisotropy throughout the full crust, or in the upper (Layer 1), middle (Layer 3) or lower (Layer 4) crust. We set anisotropy in the full-crust case to 3% with a slow axis of symmetry in either α or β , or in both wavespeeds (B or E = -0.03). A fourth type of anisotropy was defined with B = E = -0.03 and C = -0.01. The proportion C/B ~ 0.33 follows the estimates for mica-rich rocks

32 Anisotropic Crustal Models

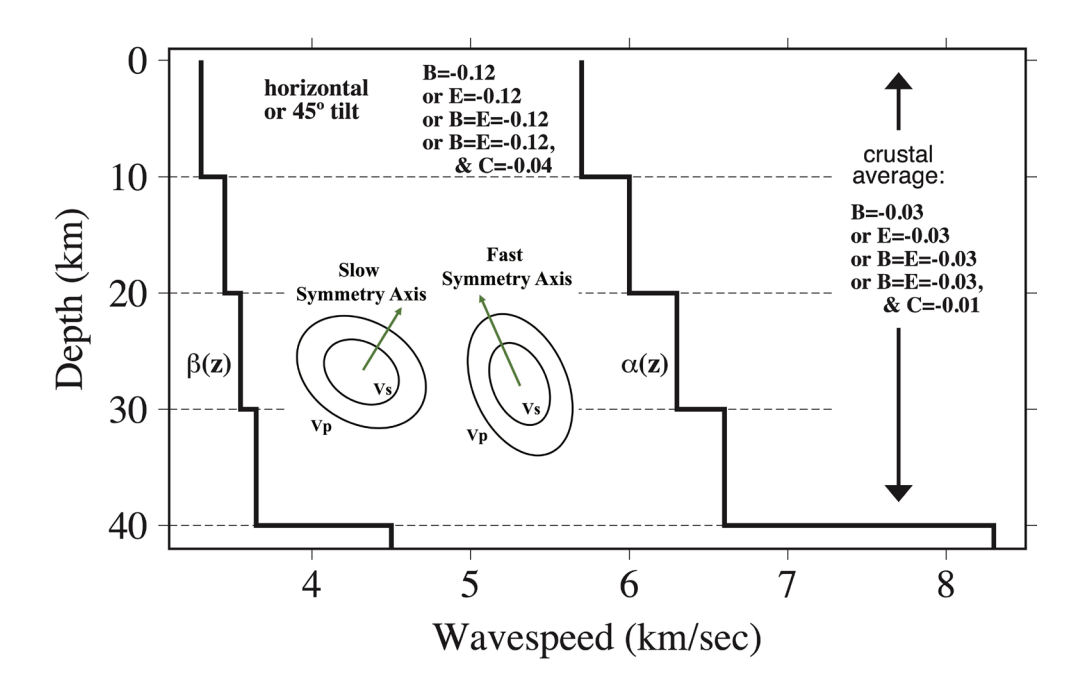


Figure 1. Parameter choices for Ps-splitting simulations in anisotropic crustal models. The anisotropic geometry possesses a symmetry axis that is either horizontal ($\psi=90^\circ$) or tilted $\psi=45^\circ$ from the vertical. In all cases the symmetry axis strike is $\theta=45^\circ$ azimuth, measured clockwise from north. Anisotropy is prescribed either in Layers 1, 3 or 4, referred to as "upper", "middle" and "lower" crust, respectively. Another option is a uniform anisotropy throughout the crust. The anisotropies tested include compression-only, shear-only, compression-shear combined with elliptical wavespeed variation (C = 0) and non-elliptical compression-shear with B/C proportions consistent with Brownlee et al. [2017]. All anisotropies have slow-axis geometry, appropriate for most crustal rocks. Single-layer anisotropy values are scaled to match the birefringence of the uniform-crust model. Azimuthal velocity variation for slow- and fast-axis anisotropy is indicated by the cartoon inset, in which the green arrow aligns with the axis of symmetry.

from Brownlee et al. [2017]. For anisotropy restricted to a single 10-km layer within the crust, we set anisotropic intensity to 4 times the average-crust value to match Ps-splitting times, that is, B=E=-0.12 and C=-0.04. We note that wavespeed anisotropy of this size has been inferred in thin layers from receiver-function studies [Levin and Park, 1997; Porter et al, 2011; Park and Rye, 2019], and is consistent with rock values [Ji et al., 2015; Brownlee et al., 2017]. Mixing and matching four depth ranges for anisotropy and four combinations of Backus parameters, we also specified two geometries: a horizontal symmetry axis and a symmetry axis tilted at $\psi=45^\circ$ from the vertical. The wave-propagation effects for other tilt angles ψ are hybrids of these two cases. We specified $\theta=45^\circ$ strike for all symmetry axes, both horizontal and tilted.

For each of 32 anisotropic crustal models parameterized in Figure 1, we computed synthetic P-coda for a realistic distribution of earthquakes, using the 471-event dataset for GSN station RAYN used by Park and Levin [2016a] to simulate natural variations in epicentral distance, incidence angle, and back-azimuth clustering. We used a cosine-shaped one-sided source pulse with 1-sec period ($\xi(t) = (1-\cos 2\pi t)/2$). We estimated receiver functions with multiple-taper correlation and harmonic regression [Park and Levin, 2016a], using a moving-window moveout correction to target a specific depth for signal-to-noise enhancement [Park and Levin, 2016b]. Figure 2 displays

Uniform Crust Horizontal-Axis Shear-Only

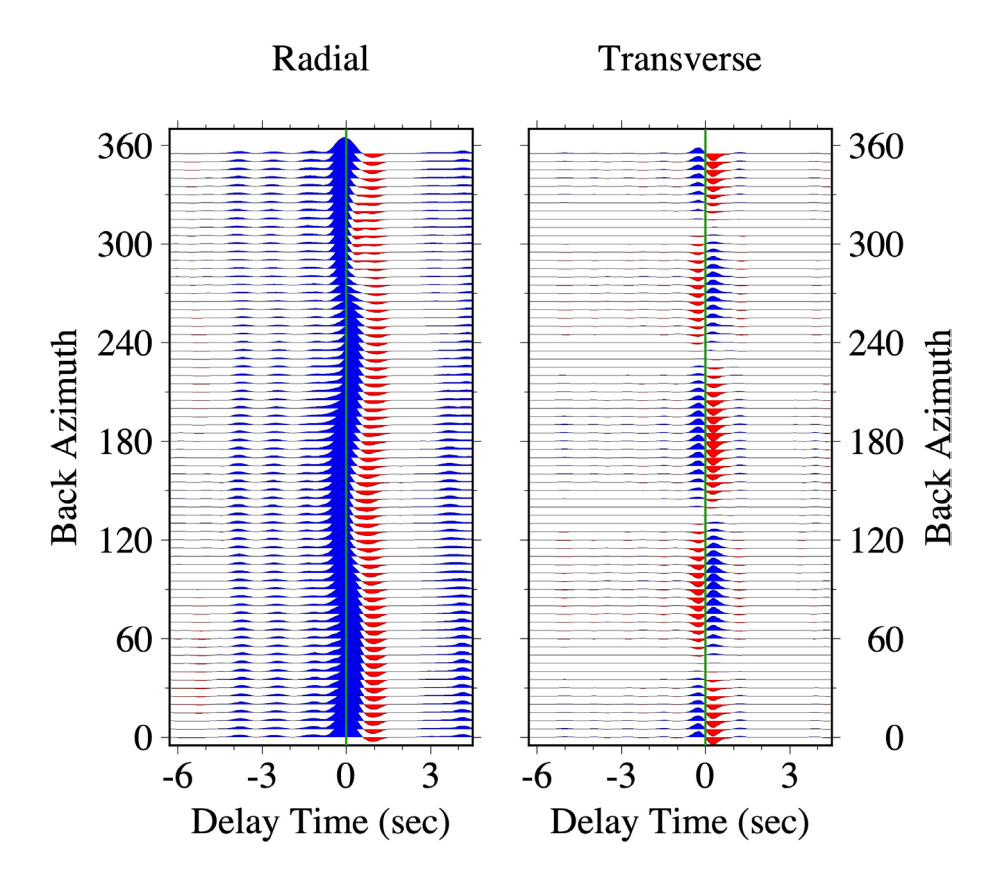


Figure 2. Back-azimuth receiver-function sweeps for synthetic seismograms in a 40-km crust with uniform E = -0.03 (3% peak-to-peak S anisotropy) with a slow horizontal symmetry axis. We use synthetic P coda from 471 earthquake locations during 1997-2005, relative to GSN station RAYN (Ar Rayn, Saudi Arabia). The RF traces are migrated by a moving-window algorithm discussed in Park and Levin [2016b] for a target depth of 40 km, the Moho depth of the model. Left panel: back-azimuth sweep of radial RFs, summing records in overlapping ξ-sectors of 10° width. The delay time of the Moho Ps conversion shifts with sinusoidal dependence on ξ. Low-amplitude positive pulses at -1.25 s, -2.5 s and -3.75 s, relative to the target depth at migrated delay time t = 0, are Ps converted waves from internal boundaries at 30-, 20- and 10-km depths, respectively. The negative pulse at +1.0 sec is a Ps_ds reverberation in the topmost layer. Right panel: back-azimuth sweep of transverse RFs. The birefringence of the Moho Ps phase is expressed with four-lobed dependence on back azimuth ξ, with pulse shape that approximates the derivative of the deconvolved Ps phase on the radial RFs.

an epicentral RF sweep of the best-fit harmonic regression over back-azimuth ξ for target depth 40 km, using the constant, $\cos \xi$, $\sin \xi$, $\cos 2\xi$, and $\sin 2\xi$ terms to interpolate the 5° spacing of RF traces across gaps in the earthquake distribution. The synthetic seismograms were rotated to LQT coordinates before processing [Vinnik, 1977], but we label the "Q" direction as "radial" in the plots to follow common terminology. Differences between radial and "Q" receiver functions are small at more than a second away from the direct-P phase.

What can these synthetic-seismogram datasets tell us about typical Ps-splitting observations? For a single seismic station and a single event, standard birefringence estimators can estimate the fast-axis azimuth φ and splitting time δt [Silver and Chan, 1991; Wüstefeld et al., 2008]. These estimators can be applied to synthetic P coda from reflectivity codes, or else can be applied to the radial and transverse receiver functions themselves. With RFs, one has ideally deconvolved the earthquake source rupture to a simple one-sided pulse [Ligorria and Ammon, 1998], which should make birefringence estimation easier. In addition, any uncertainty caused by realistic earthquake distributions can be assessed. We took the back-azimuth RF sweeps (e.g., Figure 2) and estimated fast polarization ϕ and splitting time δ t from the Moho-Ps phase in the radial and transverse RFs, taking each stacked bin about a back azimuth ξ as a separate "event." For each pair of radial and transverse RFs we searched over a grid of $(\varphi, \delta t)$ pairs in the ranges 0°-180° and 0.0-2.0 s, respectively, rotating and time-shifting to reverse the putative birefringence and to minimize the transverse variance, after Silver and Chan [1991]. We also maximized the coherence C² of the timeshifted "fast" and "slow" waveforms, similar to the cross-correlation metric of Bowman and Ando [1987], searching over the same grid to minimize the penalty metric $U(\varphi, \delta t) = (1-C^2)$. These two penalty metrics gave similar results for synthetic RFs. We plot results from the minimize-transverse metric only. With real data, analyzed in Section 7, the correlation metric returned many more non-null splitting estimates, so for real data we show birefringence estimates for both metrics.

3. Ps Splitting vs. Ps Amplitude Variation: The Best Cases

We present the back-azimuth dependence of receiver functions and their harmonic dependence for all models in the Online Supplement. In the main text of this paper we focus on a handful of models that illustrate the main waveform and birefringence behaviors of the full complement of models.

The anisotropy behind the RF traces in Figure 2 is ideal for Ps splitting: uniform shear-only anisotropy (E = -0.03, B = C = 0.00) throughout the crust with a horizontal symmetry axis. The Backus parameter E has weak influence on the Ps scattering amplitude, so the RF variation with ξ arises mostly from birefringence. Near t = 0 sec, where moveout corrections in the RFs target 40-km depth, the Moho Ps phase delay increases and decreases in the radial RF sweep in tandem with fast and slow perturbations to the SV wavespeed. In the transverse RF sweep, birefringence is expressed with the familiar "derivative pulse" shape described by Silver and Chan [1991], with a four-lobed amplitude variation in back azimuth ξ . The extremal values of Ps delay-time occur at back-azimuths ξ both parallel and normal to the symmetry axis strike (θ = 45°), where the SV wave aligns exactly with the fast or slow polarization. At these back azimuths the transverse (SH) receiver function vanishes. At RF delay-times t < 0, prior to the Moho-Ps phase, there are three weak positive pulses in the radial RFs that arise from internal crustal interfaces at 10-, 20-, and 30-km depth. Each of these crustal Ps waves suffers birefringence that influences the transverse RFs, but with amplitudes too small to be evident visually in the figure.

Figure 3 presents the harmonic regression for the seismograms analyzed in Figure 2, simulated for full-crustal E=-0.03 anisotropy with a horizontal axis. In the left panel are RF estimates for the P-to-S converted waves that are consistent with a 1-D anisotropic structure to first order, incorporating the theoretically predicted relationships of P-SV and P-SH conversion as a function of back azimuth ξ . In the right panel are RF estimates for P-to-S converted waves that are inconsistent, to first order, with a 1-D anisotropic structure. "Unmodelled" effects include Ps moveout caused by dipping interfaces and 3-D elastic structure, but there are simpler causes as well. In particular, the amplitudes of the "unmodelled" RF traces in Figure 3 arise from P-to-S amplitude variations caused by the diversity of incidence angles, caused by a diversity of epicentral distances in the realistic earthquake distribution. If velocity structure beneath a receiver involves horizontal or near-horizontal interfaces and mostly vertical elastic gradients, the "unmodelled" amplitudes will be smaller than those predicted by anisotropy or by interfaces with modest dip [Park and Levin, 2016a].

The key features of Ps splitting in Figure 3 are dual: (1) a simple pulse at t=0-sec delay on the constant term for the radial RFs, and (2) a "derivative" pulse in the sin 2ξ harmonic term. The latter feature is responsible both

Uniform Crust Horizontal-Axis Shear-Only

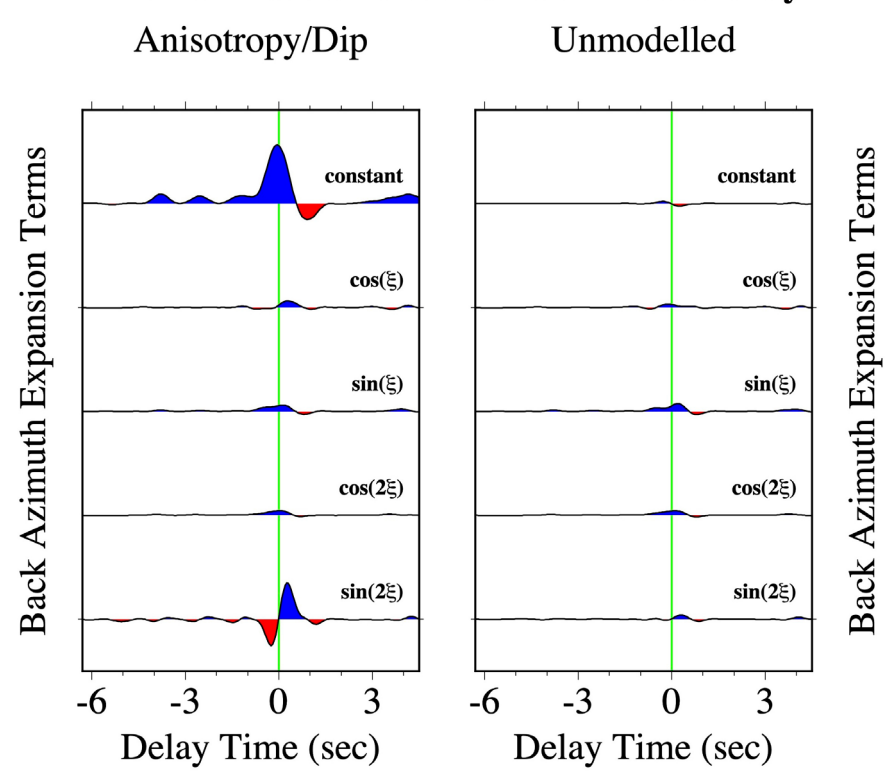


Figure 3. Harmonic terms of back azimuth ξ fit by least-squares in the frequency domain to receiver-functions estimated from synthetic seismograms in a 40-km crust with uniform E = -0.03 (3% peak-to-peak S anisotropy) with a slow horizontal symmetry axis. We use synthetic P coda from 471 earthquake locations during 1997-2005, relative to GSN station RAYN (Ar Rayn, Saudi Arabia). The RF traces are migrated by a moving-window algorithm discussed in Park and Levin [2016b] for a target depth of 40 km, the Moho depth of the model. Left panel: combinations of radial and transverse RF harmonics predicted by the first-order perturbations to Ps caused by 1-D anisotropic layering. The labels "cos(ξ)", "sin(ξ)", etc., refer to the back-azimuth dependence of the radial RF; the transverse RF is phase-shifted by 90° in ξ. The salient birefringence signal is a two-sided pulse at zero delay time on the "sin(2ξ)" harmonic. Right panel: combinations of radial and transverse RF harmonics that are not predicted by 1-D anisotropy to first order. The labels "cos(ξ)", "sin(ξ)", etc., refer to the back-azimuth dependence of the radial RF; the transverse RF is phase-shifted by -90° in ξ. The small pulses are summed from the second-order effects of varying epicentral distances P-wave incidence angles, and imperfect moveout corrections.

for shifting the delay-time of the Moho Ps wave on the radial RF as the back-azimuth sweeps through 360° , and for the 4-lobed variation of the derivative pulse on the transverse RFs. The negative-polarity pulse at t=1-sec delay, relative to the 40-km target depth, is the Ps_{MS} reverberation pulse from the top 10-km layer of the crustal model; changing the moveout correction from Ps-timing to reverberation-timing in the harmonic regression sharpens this negative pulse. This reverberation suffers a modest birefringence in the top layer, leading to a low-amplitude derivative pulse centered at t=1 sec on the sin 2ξ harmonic term.

We explored birefringence with rotations and time shifts on 6-s time windows of the RFs, centered on the Moho Ps phase. Our synthetic seismograms utilized simple pulse shapes that allowed for such wide time windows, but contained frequencies high enough for narrower time windows. Many researchers report analyzing shorter windows centered on the Ps phase [e.g., Chen et al., 2013], and most researchers report splitting times for Ps birefringence less than 0.7 sec, though not all, e.g., Xu et al. [1998]. We therefore repeated the grid searches with time windows of both 2 and 3 seconds, centered on the Ps phase, searching over splitting times $\delta t < 0.75$ sec. For synthetic-seismogram RFs longer and shorter analysis windows lead to similar results, though the shorter windows could not capture splitting times of 1 second or more. We found in real data from long-running stations (see Discussion) that the RFs were more complex, so that a 6-sec time window would typically not constrain well a fast polarization ϕ and splitting time δt . We therefore preferred shorter analysis windows (2-3 sec) for real data.

The results for the special case of a horizontal-axis shear-only anisotropy are what one expects (Figure 4), a cluster of fast axis ϕ and splitting time δt estimates around 135° azimuth (exactly 90° from the slow-axis strike $\theta = 45^{\circ}$) and 0.35-sec splitting time. As seen in the inset graph for back-azimuth $\xi = 135^{\circ}$, the few outlier estimates are likely null-splitting candidates.

Ps Splitting for Full-Crust Shear Anisotropy

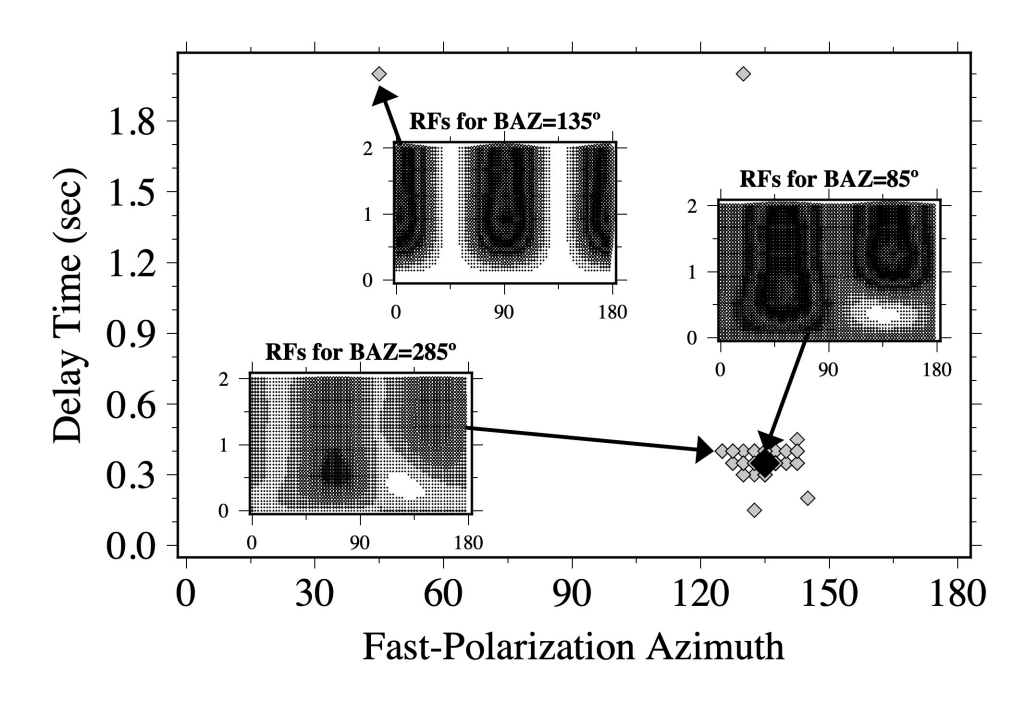


Figure 4. Ps birefringence estimates for synthetic seismograms in a 40-km crust with uniform E = -0.03 (3% peak-to-peak S anisotropy) with a slow horizontal symmetry axis. Birefringence was estimated from 72 radial/transverse receiver functions, evenly spaced in back azimuth ξ , each estimated from "events" whose RFs were summed in 10° bin-widths. Minima of the minimum-transverse penalty function are plotted as grey diamonds; many RF pairs share common minima, so overplotting is common. The black diamond is the minimum of the summed penalty-function surfaces, and should lie at the center of a cluster RF-pair minima. (It does.) The splitting penalty surfaces for three different RF pairs are plotted as insets. For back azimuths $\xi = 85^\circ$,285° the penalty-function minima are clearly seen. For back azimuths $\xi = 135^\circ$ the penalty-function minimum is indistinct, because the near-alignment of these events with the apparent anisotropic fast axis suppresses the expression of birefringence.

4. Ps Splitting vs. Ps Amplitude Variation: Realistic Cases

Ps-splitting estimates are robust to some deviations of crustal anisotropy from the simplest assumptions. P waves do not interact with the shear-anisotropy parameter E to first order [Park and Levin, 2016a], so that Ps birefringence is not disrupted much by anisotropic layering, if only shear-anisotropy is present. For example, concentrating shear-anisotropy into a single crustal layer does not disrupt the measured Ps splitting when anisotropy has a horizontal symmetry axis; the path-average birefringence is unchanged and E has weak influence on P-to-S conversion amplitudes. If the symmetry axis is tilted, the birefringence pattern retains its four-lobed radiation pattern in the Moho Ps phase but adds two-lobed harmonics from modest P-to-S amplitude effects. Ps birefringence in a dipping-axis model exhibits smaller splitting times δt for the same anisotropy strength, by roughly half. Consistent with Sileny and Plomerova [1996], the splitting parameters also have greater variance about their mean values, suggesting weaker constraints on the crustal fast polarization ϕ for data sets where the number of individual Ps splits is limited. Restriction of tilted-axis anisotropy to a single 10-km layer adds Ps amplitude variations from P-to-S conversions at intra-crustal interfaces. For example, the major RF signatures of Ps birefringence are readily seen in RF back-azimuth profiles for tilted-axis anisotropy concentrated in the 10-km lower crustal layer (Figure 5).

Lower Crust Tilted-Axis Shear-Only

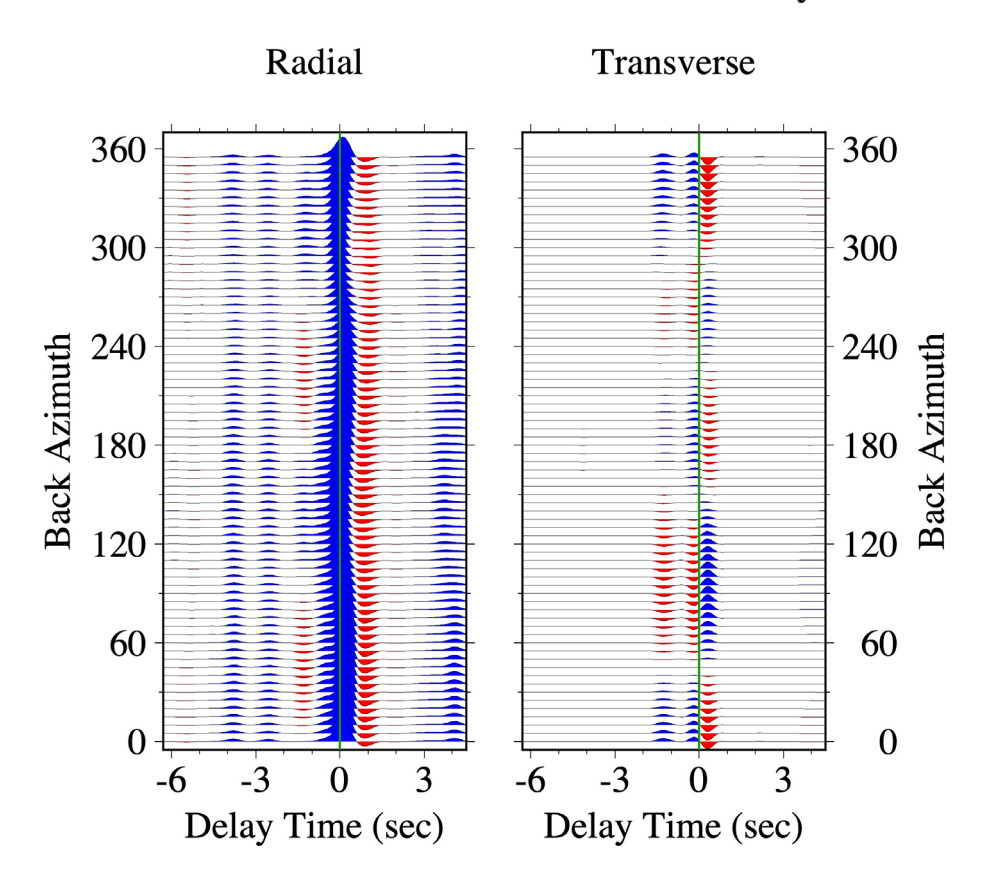


Figure 5. Back-azimuth receiver-function sweeps for synthetic seismograms in a 40-km crust with E=-0.12 (12% peak-to-peak S anisotropy) with a slow 45°-tilted symmetry axis in the lowermost 10 km of the crust. Synthetic seismograms for 471 earthquake locations were processed and plotted in a manner similar to Figure 2. Left panel: back-azimuth sweep of radial RFs, summing records in overlapping ξ-sectors of 10° width. The delay time of the Moho Ps conversion shifts with sinusoidal dependence on ξ. Low-amplitude positive pulses at -2.5 s and -3.75 s, relative to the target depth at migrated delay time t=0, are Ps converted waves from internal boundaries at 20- and 10-km depths, respectively. The Ps conversion at -1.25 s, from the 30-km interface, has sinusoidal amplitude, owing to P-to-SV amplitude variations induced by lower-crust anisotropy. The negative pulse at +1.0 sec is a Ps_ds reverberation in the topmost layer. Right panel: back-azimuth sweep of transverse RFs. The birefringence of the Moho Ps phase is expressed with four-lobed dependence on back azimuth ξ, with pulse shape that approximates the derivative of the deconvolved Ps phase on the radial RFs. In addition, a pulse with sinusoidal amplitude can be found at -1.25 s relative to the Moho Ps pulse, and is associated with P-to-SH conversions induced by lower-crust anisotropy.

Outlier estimates of splitting parameters become much more common in this case (Figure 6), even for these noise-free synthetic seismograms.

Outside theoretical models, all anisotropic crustal lithologies possess compressional anisotropy in addition to shear, e.g., Ji et al. [2015]. The compressional anisotropy parameter B does not influence birefringence splitting times directly. However, if only B is nonzero or we scale the Backus parameters B and E together, the anisotropy has significant influence on P-to-S conversion amplitudes if the symmetry axis is horizontal (Figure 7), and larger influence for a tilted symmetry axis (Figure 8). For horizontal and tilted symmetry axes, Ps amplitudes scale with the horizontal and vertical slownesses, respectively, of the incoming P wave [Park and Levin, 2016a]. Practically speaking, this slowness dependence means that steeply-incident body waves, such as deep-mantle P and PKP phases, will scatter into four-lobed Ps patterns with small amplitude, and scatter into 2-lobed patterns with large amplitude. For body-waves whose incidence is shallow, whether for body waves that bottom in the upper mantle or that approach a dipping interface from its downdip side, the amplitudes of the 4-lobed and 2-lobed Ps scattered

waves become more similar. Most P phases used in RF studies are steeply incident, and so will scatter more strongly with tilted-axis anisotropy.

If the shear and compressional anisotropies are uniform within the crust, estimates of Ps splitting from the RFs can remain unbiased estimators of the average fast-polarization φ . However, if the anisotropy is concentrated in a single crustal layer, the P-to-S converted waves from the top and bottom of this layer can appear to a birefringence estimator as the fast and slow polarizations, with a splitting time δt that scales with the thickness of the layer (Figure 9). The fast-polarizations φ estimated from these RFs, however, do not cluster around a mean value, and instead return values that drift with back azimuth ξ (Figure 9). Estimates of shear birefringence through two mis-aligned anisotropic layers also display fast polarizations φ that drift with back azimuth ξ [Silver and Savage, 1994; Levin et al., 1999]. Therefore, an incorrect interpretation of the anisotropy seems likely if only Ps-splitting observations are used.

Ps Splitting for Lower-Crust Tilted-Axis Shear Anisotropy

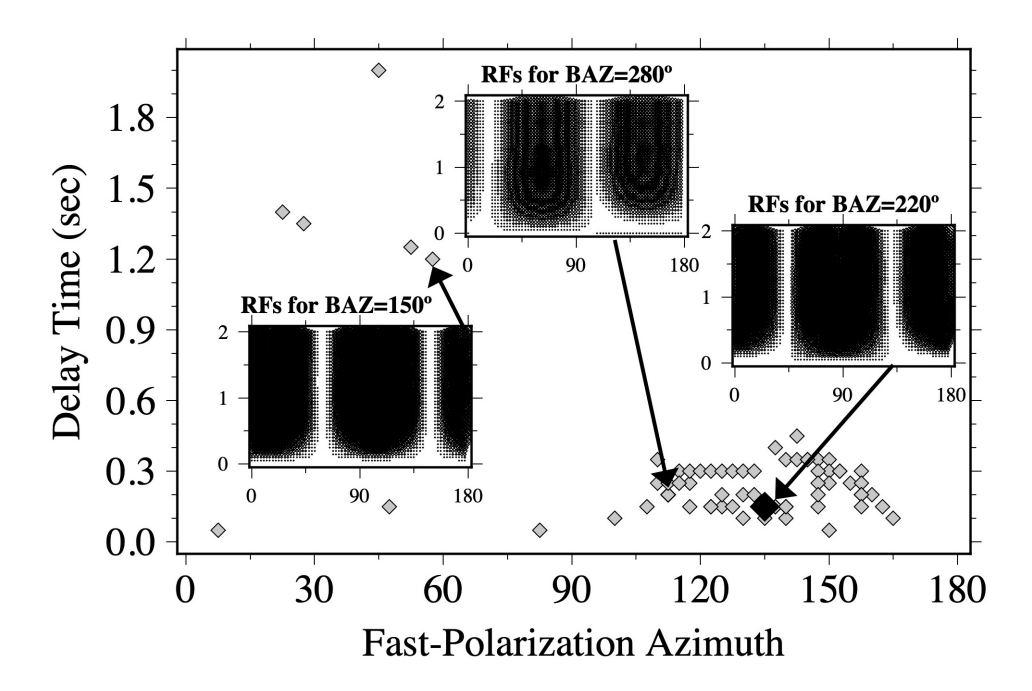


Figure 6. Ps birefringence estimates for synthetic seismograms in a 40-km crust with E=-0.12 (12% peak-to-peak S anisotropy) with a slow 45° -tilted symmetry axis in the lowermost 10 km of the crust. Synthetic seismograms for 471 earthquake locations were processed and plotted in a manner similar to Figure 4. Minima of the minimum-transverse penalty function are plotted as grey diamonds. The black diamond is the minimum of the summed penalty-function surfaces, and should lie at the center of a cluster RF-pair minima. The splitting penalty surfaces for three different RF pairs are plotted as insets. For all selected back azimuths ξ the penalty-function minima are weakly expressed relative to the anisotropic geometry analyzed in Figure 4, so that the birefringence estimates scatter around average values that match model predictions.

Middle Crust Horizontal-Axis B=E=-0.12

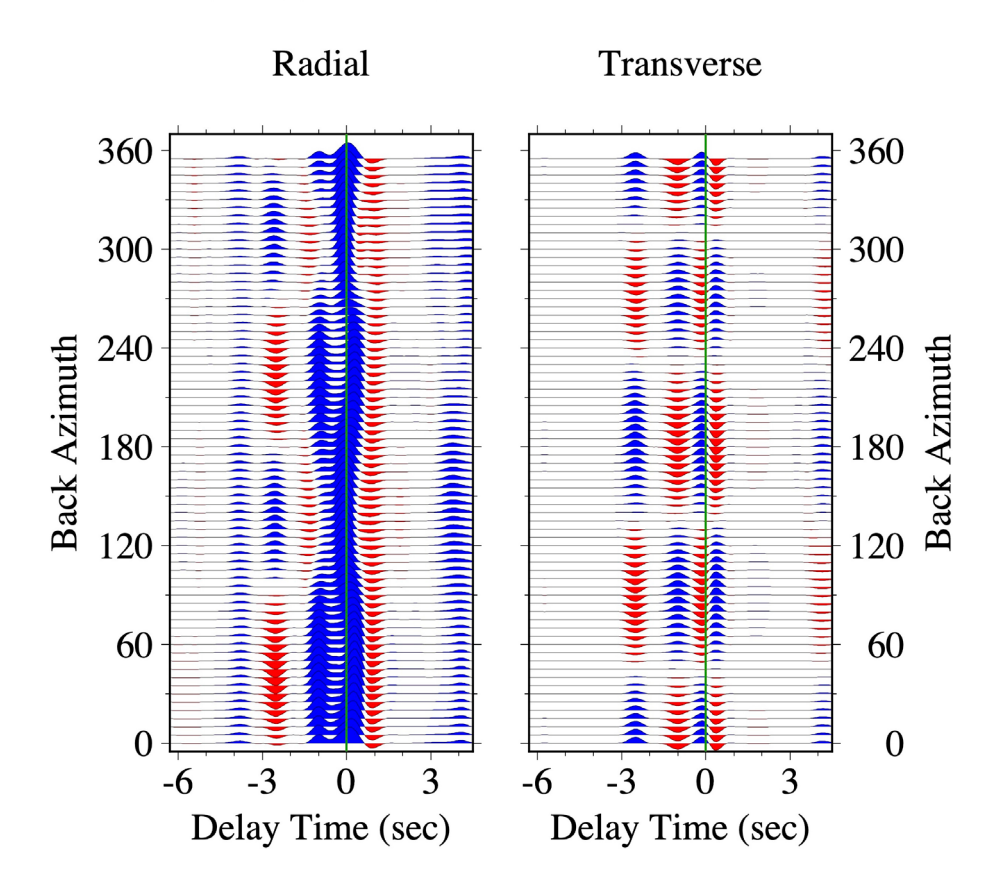


Figure 7. Back-azimuth receiver-function sweeps for synthetic seismograms in a 40-km crust with B=E=-0.12 (12% peak-to-peak P and S anisotropies) with a slow horizontal symmetry axis in the middle crust. Synthetic seismograms for 471 earthquake locations were processed and plotted in a manner similar to Figure 2. Left panel: back-azimuth sweep of radial RFs, summing records in overlapping ξ -sectors of 10° width. The delay time of the Moho Ps conversion shifts with sinusoidal dependence on ξ . Medium-amplitude pulses at -2.5 s and -1.25 s, relative to the target depth at migrated delay time t=0, are Ps converted waves from internal boundaries at 20- and 30-km depths, respectively. These pulses vary sinusoidally in amplitude with back azimuth ξ , owing to P-to-SV amplitude variations induced by middle-crust anisotropy. The negative pulse at +1.0 sec is a Ps_ds reverberation in the topmost layer. Right panel: back-azimuth sweep of transverse RFs. The birefringence of the Moho Ps phase is expressed with four-lobed dependence on back azimuth ξ , with pulse shape that approximates the derivative of the deconvolved Ps phase on the radial RFs. This birefringence signal is preceded by medium-amplitude, sinusoidally-varying pulses at -2.5 s and -1.25 s, from P-to-SH converted waves from internal boundaries at 20- and 30-km depths, respectively.

Middle Crust Tilted-Axis B=E=-0.12

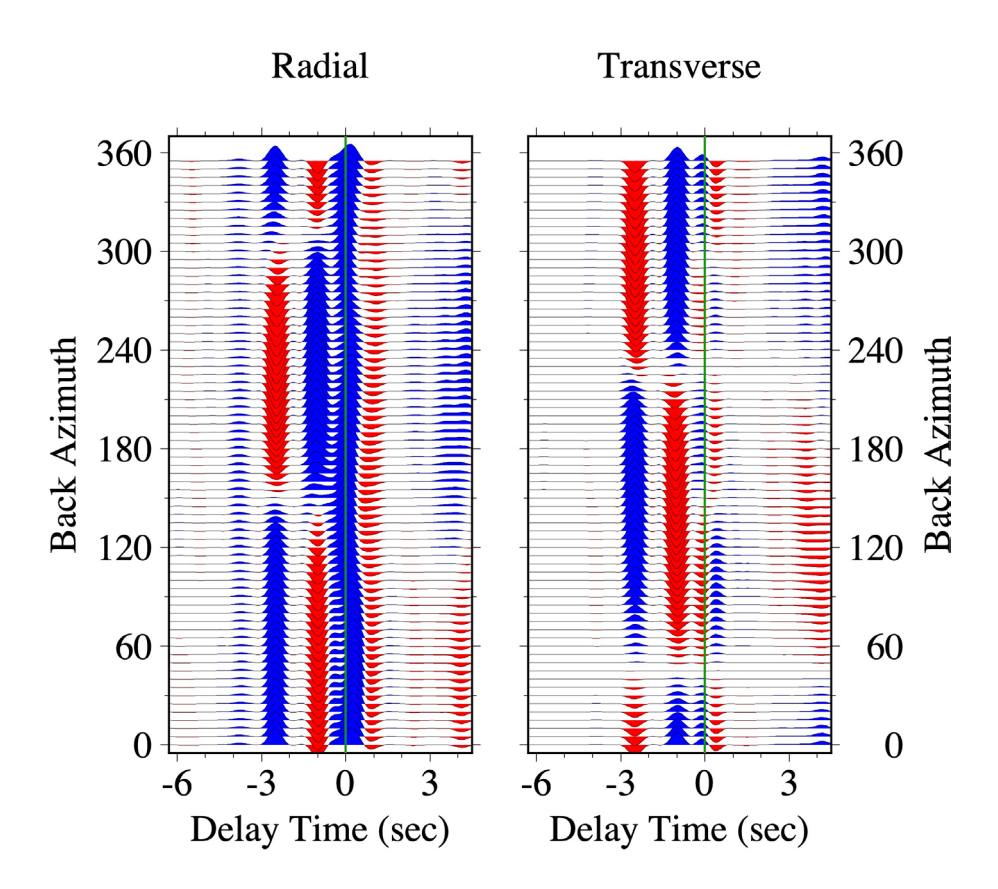


Figure 8. Back-azimuth receiver-function sweeps for synthetic seismograms in a 40-km crust with B = E = -0.12 (12% peak-to-peak P and S anisotropies) with a slow 45°-tilted symmetry axis in the middle crust. Synthetic seismograms for 471 earthquake locations were processed and plotted in a manner similar to Figure 2. Left panel: back-azimuth sweep of radial RFs, summing records in overlapping ξ-sectors of 10° width. The delay time of the Moho Ps conversion shifts with sinusoidal dependence on ξ. High-amplitude pulses at -2.5 s and -1.25 s, relative to the target depth at migrated delay time t = 0, are Ps converted waves from internal boundaries at 20- and 30-km depths, respectively. These pulses vary sinusoidally in amplitude with back azimuth ξ, owing to P-to-SV amplitude variations induced by middle-crust anisotropy. The negative pulse at +1.0 sec is a Ps_ds reverberation in the topmost layer. Right panel: back-azimuth sweep of transverse RFs. The birefringence of the Moho Ps phase is expressed with four-lobed dependence on back azimuth ξ, with pulse shape that approximates the derivative of the deconvolved Ps phase on the radial RFs. This birefringence signal is preceded by high-amplitude, sinusoidally-varying pulses at -2.5 s and -1.25 s, from P-to-SH converted waves from internal boundaries at 20- and 30-km depths, respectively.

Ps Splitting for Middle-Crust Tilted-Axis Mixed Anisotropy

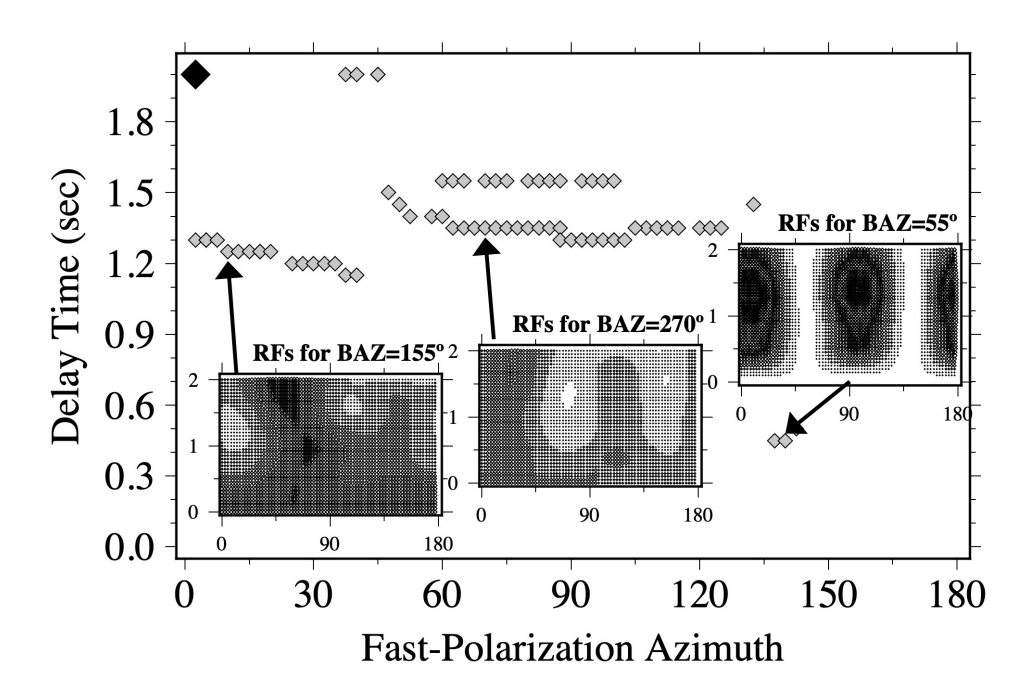


Figure 9. Ps birefringence estimates for synthetic seismograms in a 40-km crust with B=E=-0.12 (12% peak-to-peak P and S anisotropies) with a slow 45°-tilted symmetry axis in the middle of the crust. Synthetic seismograms for 471 earthquake locations were processed and plotted in a manner similar to Figure 4. Minima of the minimum-transverse penalty function are plotted as grey diamonds. The black diamond is the minimum of the summed penalty-function surfaces. The fast polarization φ and splitting times δ t of the minima disperse widely with back azimuth ξ , and the aggregated penalty-function lacks a useful minimum. The splitting penalty surfaces for three different RF pairs are plotted as insets. For back azimuth $\xi = 55^\circ$ the penalty-function minimum is indistinct, but the penalty surfaces for $\xi = 155^\circ$ and 270° are deceptively localized, and far from the true values of model fast polarization φ and splitting time δ t.

5. The Effects of Backus Parameter C

The extension of our anisotropic models to the Backus parameter C leads to significant, but not dramatic, changes in receiver-function amplitudes, consistent with modest deviations from ellipsoidal wavespeed variation as a function of the angle ζ from the symmetry axis [Brownlee et al., 2017]. Figure 10 compares harmonic-expansion terms of the receiver functions computed for tilted-axis anisotropy in the middle layer of the crust, comparing cases with C=0 and nonzero C. Close inspection of the figure reveals features that would alter key interpretations of the harmonic-expansion terms. For example, the parameter C magnifies the amplitudes of the 2-lobed Ps scattering from the top and bottom of the anisotropic layer and contributes significant positive and negative pulses that are constant with back azimuth. If the effect of C were neglected, we would interpret the Backus parameters B and E to be larger than specified in the model. We would also infer two large jumps in isotropic wavespeeds, one positive and one negative, within the middle crust.

The Backus parameter C is defined by compressional wavespeed, but it also influences SH wavespeed, and S-wave propagation more generally. In Figure 10, nonzero C alters the 4-lobed Ps amplitude variation of the Moho Ps phase. As seen in Figure 3, the derivative pulse that characterizes the sin 2ξ term at t=0 sec, i.e., at the 40-km target depth, includes and explains the fast and slow Ps waves and their birefringence. This characteristic RF pulse is prominent in Figure 10 for C=0, but nearly absent for C=-0.04, the value consistent for mica-rich rocks. In the same harmonic term for C=-0.04 a new derivative pulse appears at t=-1.3 sec, coincident with the Ps converted phase at 30-km depth, the bottom interface of the anisotropic layer. This 30-km Ps phase is not birefringent in the normal sense, because the isotropic portion of the Ps phase from this interface has low amplitude. In effect, the birefringence of the Moho Ps phase is greatly reduced by nonzero C, and some of the birefringence effect transfers to Ps from a

shallower interface. We verified that this comparative effect is also seen for RFs estimated for crustal models with BE and BCE prescribed in the upper layer. The Ps-splitting effect of the parameter C appears to be strongest for anisotropy with a tilted symmetry axis; anisotropy comparisons for models with a horizontal symmetry axis do not exhibit it, e.g., the left panel of Figure 10.

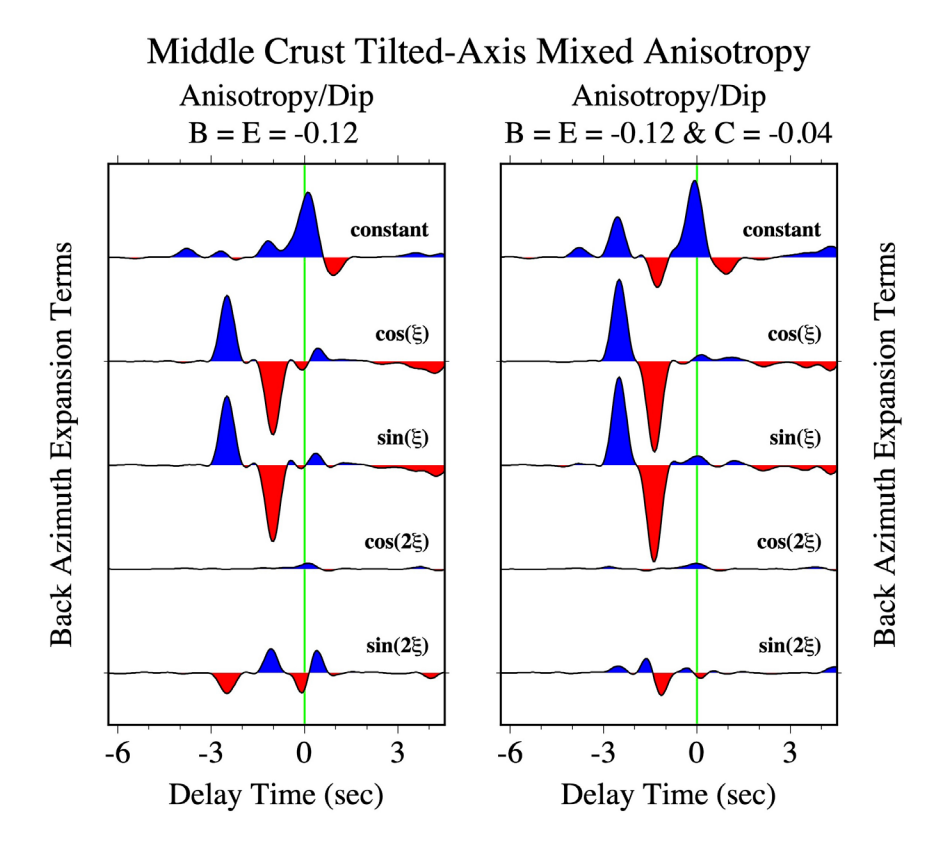


Figure 10. Harmonic terms of back azimuth ξ fit by least-squares in the frequency domain to receiver-functions estimated from synthetic seismograms in a 40-km crust with either B=E=-0.12 (12% peak-to-peak P and S anisotropies) with a slow 45°-tilted symmetry axis, or a model with similar geometry and Backus parameters B=E=-0.12 and C=-0.04. Synthetic seismograms from 471 epicenters were processed and plotted in a manner similar to Figure 3. Left panel: for the B=E=-0.12 model, combinations of radial and transverse RF harmonics predicted by the first-order perturbations to Ps caused by 1-D anisotropy. The labels "cos(ξ)", "sin(ξ)", etc., refer to the back-azimuth dependence of the radial RF; the transverse RF is phase-shifted by 90° in ξ . Note the high-amplitude pulses at -2.5 s and -3.75 s on the "sin(ξ)" and "cos(ξ)" harmonic traces, caused largely by tilted-axis P anisotropy. Right panel: for the B=E=-0.12, C=-0.04 model, combinations of radial and transverse RF harmonics predicted by the first-order perturbations to Ps caused by 1-D anisotropic layering. Plotting conventions identical to the left panel. The effects of the non-elliptical wavespeed parameter C include substantial positive and negative pulses in the constant term, and a time shift of the 2-sided birefringence pulse on the "sin(2ξ)" harmonic.

6. The Ambiguity of a Thin Basal Crust Layer

Another geologic scenario to consider is a thin anisotropic basal layer in the crust with elasticity that deviates markedly from crustal properties, either as a low-velocity channel from underplated schists, serpentinites or metasediments [Porter et al., 2011; Nikulin et al., 2009], or as a high-velocity layer above the Moho that interpolates crust and mantle properties [Levin and Park, 1997; Olugboji and Park, 2016; Park and Rye, 2019]. We modify the previous models (Figure 1) to specify a 5-km anisotropic basal layer with either low or high wavespeed and a horizontal or tilted symmetry axis. We specify B = E = -0.12. Some plausible rocks within a basal layer could have foliation with a fast-axis, e.g., Bernard and Behr [2017]; this would change the polarity of some RF signals, but not the general behavior. Other layers in the models are isotropic (Figure 11). For these geometries, a seismometer records two Ps converted waves, from the top and bottom of the basal layer (Figure 12). For the sin 2ξ RF-harmonic terms there is a "derivative pulse" near t = 0 whose shape resembles that of birefringence in Figure 3. Although some Ps birefringence occurs within the basal layer, this pulse is controlled largely by the basal layer thickness.

Four Anisotropic Basal-Layer Models

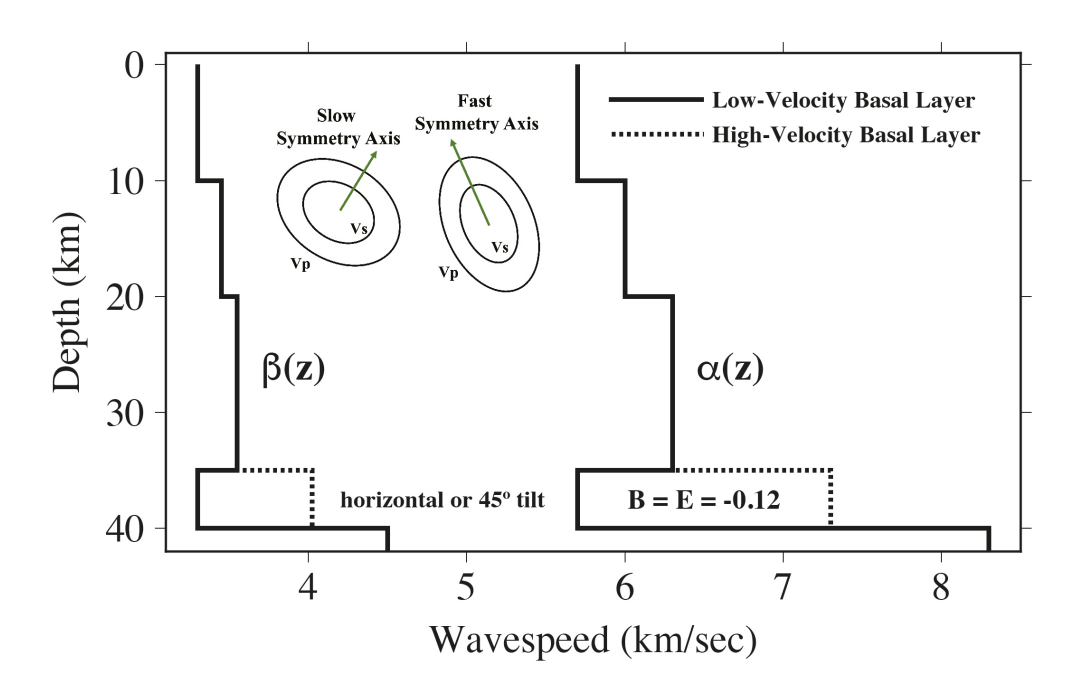


Figure 11. Parameter choices for Ps-splitting simulations in anisotropic crustal models with a basal crustal layer. The anisotropic geometry possesses a symmetry axis that is either horizontal ($\psi=90^\circ$) or tilted $\psi=45^\circ$ from the vertical. In all cases the symmetry axis strike is $\theta=45^\circ$ azimuth, measured clockwise from north. Anisotropies are prescribed only in the 5-km basal layer, which has seismic velocities that are either substantially lower (solid line) or substantially higher (dotted line) than the lower crust. All anisotropies have slow-axis geometry, appropriate for most crustal rocks, and B=E=-0.12 (12% peak-to-peak anisotropy in P and S wavespeeds). Azimuthal velocity variation for slow- and fast-axis anisotropy is indicated by the cartoon inset, in which the green arrow aligns with the axis of symmetry.

The question we ask is, will a birefringence estimator interpret the Ps phases from separate interfaces as fast and slow shear polarizations, with an apparent splitting time $\delta t = H/(1/\beta - 1/\alpha)$ that scales with the thickness H of the layer, and not with the real splitting time in the layer? Figure 13 shows that our answer is yes, in the cases we examine. For horizontal-axis anisotropy in a high-velocity basal layer, the splitting estimates from the RF back-azimuth sweeps cluster within 15° of the correct fast-axis azimuth ($\phi = 135$ °), but estimate the splitting time as the differential P-S traveltime through the layer (0.55 s) rather than the true splitting time ($\delta t = 0.2$ s). Birefringence estimates of the back-azimuth RF sweep for the tilted-axis models also return apparent splitting times

 $\delta t \sim 0.55$ -0.65 s, but with no agreement on the fast polarization ϕ . This δt is consistent with the differential travel time between P and S waves through the basal layer. It does not match the predicted splitting time δt of roughly 0.2 s. Despite the overall disagreement on fast polarization ϕ in the birefringence estimates, each estimate is based on a persuasive minimum in the pseudo-transverse-RF amplitude (Figure 14). Estimates of crustal-average anisotropy from a single or a few Ps-splitting estimates would be unreliable in this scenario.

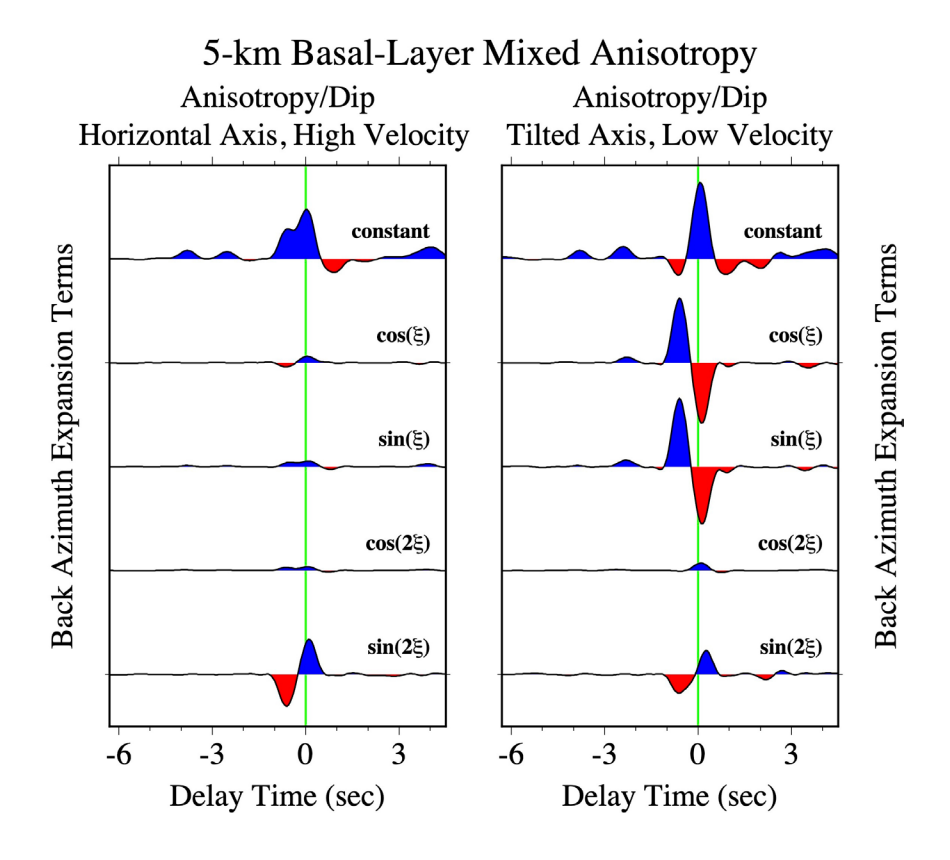


Figure 12. Harmonic terms of back azimuth ξ fit by least-squares in the frequency domain to receiver-functions estimated from synthetic seismograms in a crustal model with B=E=-0.12 (12% peak-to-peak P and S anisotropies) with either a slow horizontal symmetry axis high-velocity basal crustal layer (left panel), or a slow 45°-tilted symmetry axis low-velocity basal layer (right panel). Synthetic seismograms from 471 epicenters were processed and plotted in a manner similar to Figure 3. Both panels display combinations of radial and transverse RF harmonics predicted by the first-order perturbations to Ps caused by 1-D anisotropy. The labels "cos(ξ)", "sin(ξ)", etc., refer to the back-azimuth dependence of the radial RF; the transverse RF is phase-shifted by 90° in ξ . For both panels, the two-sided pulse on the "sin(2ξ)" harmonic is not caused by birefringence of the Moho Ps phase, but rather by the P-to-SV and P-to-SH converted phases at the top and bottom of the basal layer.

Ps Splitting for Basal HVZ Horizontal-Axis Mixed Anisotropy

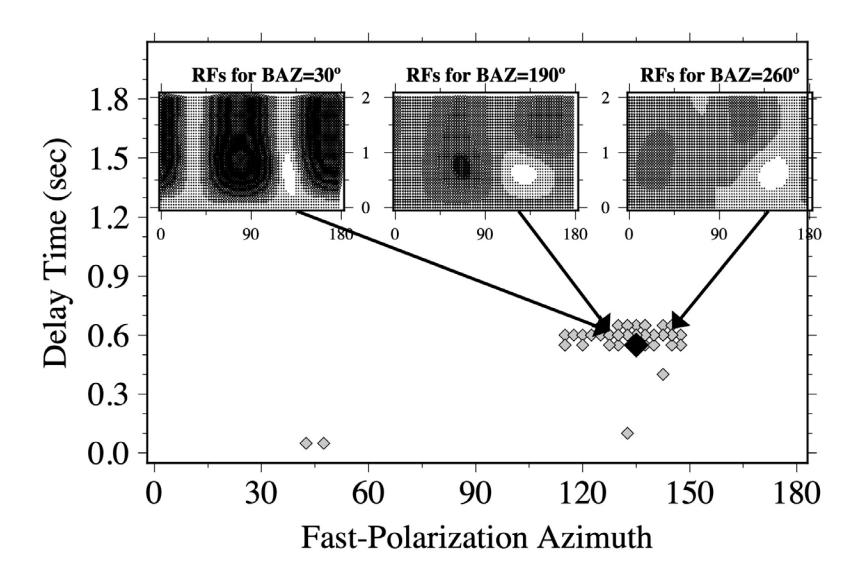


Figure 13. Ps birefringence estimates for synthetic seismograms in a 40-km crust with B=E=-0.12 (12% peak-to-peak P and S anisotropies) with a slow horizontal symmetry axis in a 5-km thick high-velocity basal layer. Synthetic seismograms for 471 earthquake locations were processed and plotted in a manner similar to Figure 4. Minima of the minimum-transverse penalty function are plotted as grey diamonds. The black diamond is the minimum of the summed penalty-function surfaces. The splitting penalty surfaces for three different RF pairs are plotted as insets; all display distinct penalty-function minima. Despite the appearance of a consistent result, similar to Figure 4, the splitting time is incorrect by a factor of roughly two. The true value of model fast polarization ϕ agrees with the black diamond, but the inferred splitting time δ t corresponds to the time delay between Ps conversions at the top and bottom of the basal layer.

Ps Splitting for Basal LVZ Tilted-Axis Mixed Anisotropy

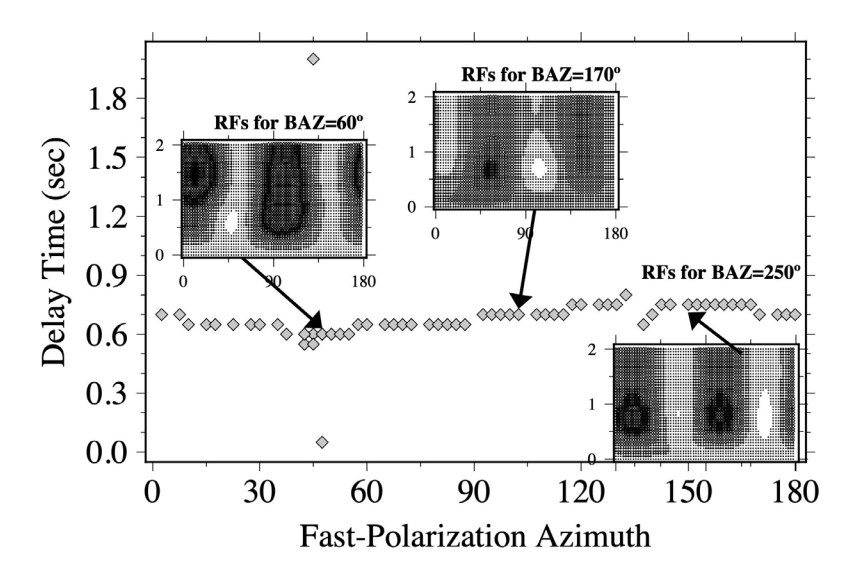


Figure 14. Ps birefringence estimates for synthetic seismograms in a 40-km crust with B=E=-0.12 (12% peak-to-peak P and S anisotropies) with a slow horizontal symmetry axis in a 5-km thick high-velocity basal layer. Synthetic seismograms for 471 earthquake locations were processed and plotted in a manner similar to Figure 4. Minima of the minimum-transverse penalty function are plotted as grey diamonds. The splitting penalty surfaces for three different RF pairs are plotted as insets; all display distinct penalty-function minima whose fast polarizations ϕ disagree. The apparent splitting time approximates the time delay between Ps conversions at the top and bottom of the basal layer.

7. Ps Splitting at Selected Permanent Stations

We applied the modelling tools developed in this paper to data from selected long-running stations in the Global Seismographic Network [Butler et al., 2004], stations ARU (Arti, Russia), LSA (Lhasa Tibet, China) and RAYN (Ar Rayn, Saudi Arabia), whose receiver functions have been studied previously [Levin and Park, 2000; Park and Levin, 2016ab; Liu and Park, 2017]. Categorical conclusions about global datasets cannot be made from a handful of stations, but we find evidence in each location for some of the biases and complications of Ps splitting that we find in the synthetic experiments. We used shorter time windows to estimate Ps splitting relative to synthetic RFs, so penalty functions are graphed only for 0 δ t < 0.75. We also found that estimates of ϕ and δ t diverged significantly between the minimum-transverse and coherence penalty metrics, so we plotted both.

GSN_Station_RAYN

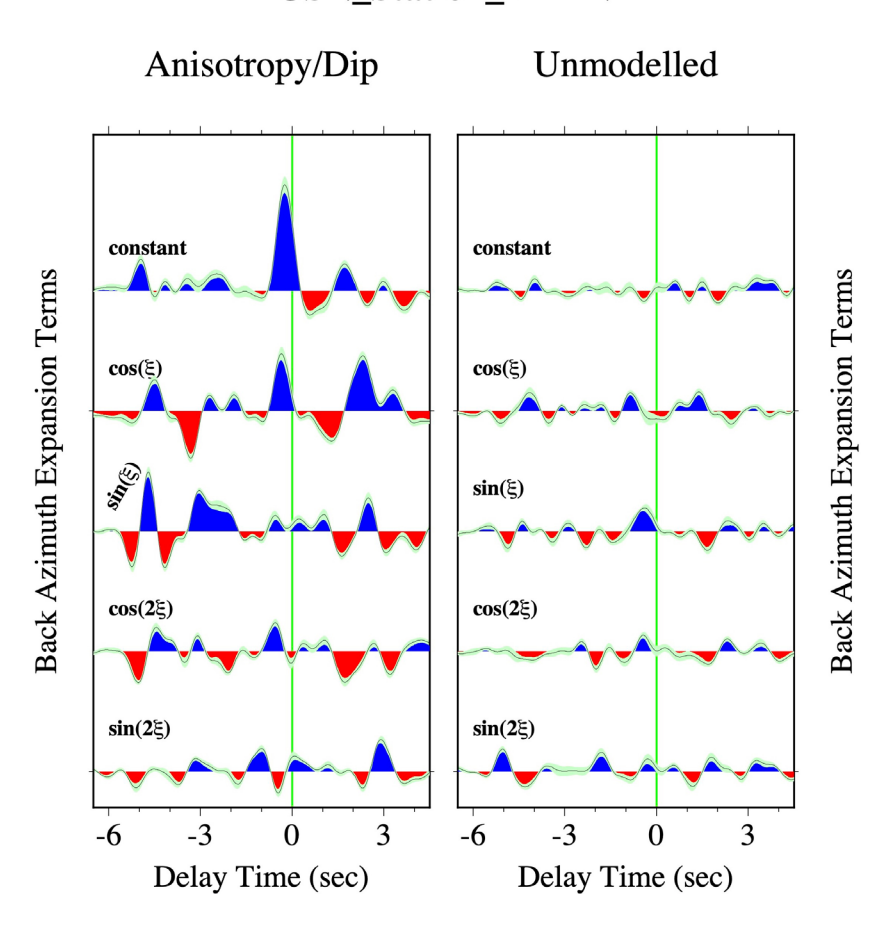


Figure 15. Harmonic terms of back azimuth ξ fit by least-squares in the frequency domain to receiver-functions estimated from 471 earthquakes, with magnitude 6.0 or more, recorded during 1997-2005 at GSN station RAYN (Ar Rayn, Saudi Arabia). The RF traces are migrated by a moving-window algorithm discussed in Park and Levin [2016b] for a target depth of 40 km. Bootstrap uncertainties are indicated with green. Left panel: combinations of radial and transverse RF harmonics predicted by the first-order perturbations to Ps caused by 1-D anisotropic layering. The labels " $\cos(\xi)$ ", " $\sin(\xi)$ ", etc., refer to the back-azimuth dependence of the radial RF; the transverse RF is phase-shifted by 90° in ξ . The inferred Moho Ps conversion sits near 0-s delay time on the "constant" harmonic, and is accompanied by a substantial one-sided pulse on the " $\cos(\xi)$ " harmonic. A smaller two-sided pulse on the " $\sin(2\xi)$ " harmonic resembles the birefringence signal in Figure 2. Right panel: combinations of radial and transverse RF harmonics that are not predicted by 1-D anisotropy to first order. The labels " $\cos(\xi)$ ", " $\sin(\xi)$ ", etc., refer to the back-azimuth dependence of the radial RF; the transverse RF is phase-shifted by -90° in ξ . These RF combinations have small amplitudes, but are not negligible, when compared to harmonic combinations consistent with 1-D anisotropy.

The harmonic decomposition of the RAYN dataset analyzed by Park and Levin [2016a] is graphed in Figure 15 with bootstrap uncertainties, which are modest. The other uncertainty indicators are the "unmodelled" RF harmonic combinations, which combine radial and transverse RFs in a combination that is not predicted by 1-D wave propagation. Relative to the targeted 40-km depth, the Moho Ps delay time lies close to t=-0.2 sec and exhibits a large two-lobed amplitude variation. At t=2.2 sec relative to the target depth, another two-lobed feature is prominent but lacks a significant constant term. This suggests a sharp transition in anisotropy at \sim 70-km depth, with negligible change in isotropic wavespeed. Levin and Park [2000] identified this feature with the lithospheric Hales discontinuity, a possible strain artifact of Precambrian continental assembly.

We analyzed splitting for the two Ps phases, produced by the Moho and by the nominal Hales discontinuity. Estimates of Ps-splitting parameters for each Ps phase are inconclusive. Figure 16 displays results for the Moho Ps phase. For Ps conversions at both depths, there are sine-wave signals with 4-lobed back-azimuth variation near both phases, which could be a key marker of Ps birefringence. However, the largest RF signals are dominated by two-lobed ξ variation, a feature that disrupts Ps-splitting estimates in our synthetics tests. For RAYN this behavior in synthetic RFs is also seen; no clustering of fast-axis orientation ϕ and splitting time δ t is found for either Ps phase analyzed. The minimum-transverse penalty function [Silver and Chan, 1991] fails to isolate a penalty function minimum with δ t < 0.7 s for RFs at most back azimuths. Absent or weak minima are also found when longer time windows, which allow longer splitting times, are used in the analysis. There are more penalty-function minima with δ t < 0.7 s for RFs when we use the coherence metric [Bowman and Ando, 1987], but these minima do not cluster well around average values of δ t and ϕ .

Ps Splitting for GSN Station RAYN

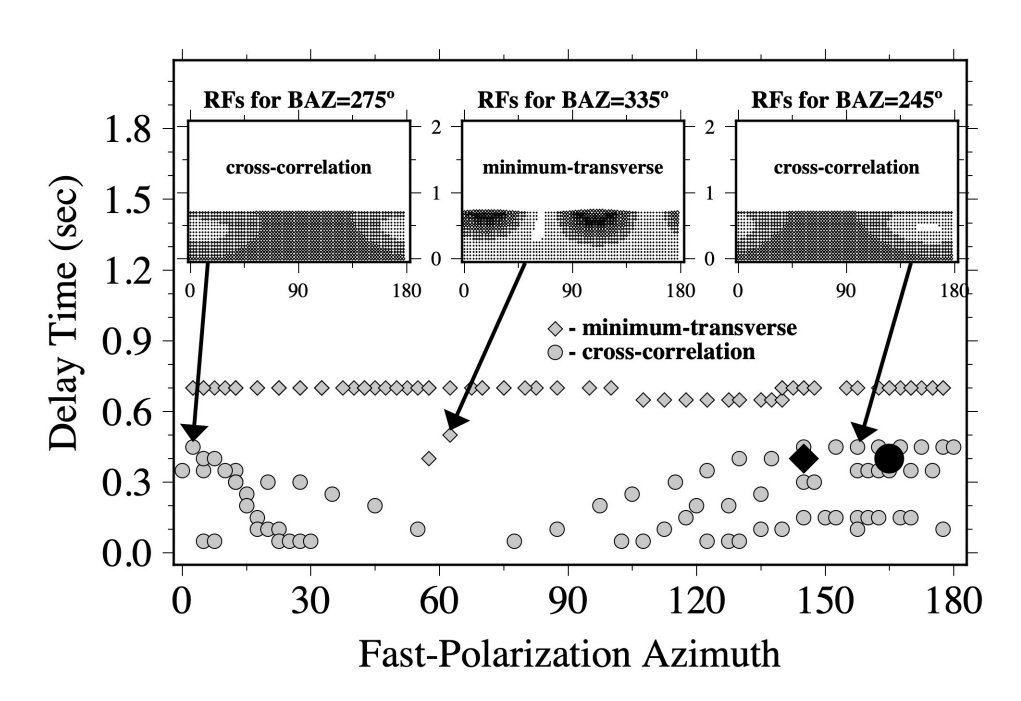


Figure 16. Ps birefringence estimates estimated from 471 earthquakes recorded during 1997-2005 at GSN station RAYN (Ar Rayn, Saudi Arabia). Seismograms were processed and plotted in a manner similar to Figure 4, but with 2-second data windows centered on the inferred Moho Ps phase, with splitting times restricted to $\delta t < 0.75$ s. Minima of the minimum-transverse penalty function are plotted as grey diamonds. Minima of the cross-correlation penalty function are plotted as grey circles. The black diamond is the minimum of the summed minimum-transverse penalty-function surfaces. The black circle is the minimum of the summed cross-correlation penalty-function surfaces. The splitting penalty surfaces for three different RF pairs are plotted as insets; all display distinct penalty-function minima whose fast polarizations φ disagree. The apparent splitting times for the minimum-transverse RFs typically sit at the maximum tested value ($\delta t = 0.7$ s), but δt at the minimum for the summed penalties lies near the middle of the tested range ($\delta t = 0.4$ s). The splitting times δt of the cross-correlation penalty minima are not extreme, but inferred fast polarizations φ disperse widely.

Similar behavior is evident at station ARU, where Levin and Park [1997] inferred a strongly anisotropic layer at the base of the crust, later confirmed by Park and Levin [2000] and Liu and Park [2017] with more data and better RF estimates. Figure 17 shows the harmonic decomposition of the receiver functions, showing clear evidence for two positive Ps converted waves that originate in the deep crust, each with strong two-lobed amplitude variations consistent with tilted-axis anisotropy. Similar to station RAYN, the birefringence estimates of the Ps converted phase for ARU show only a minority of cases with a reasonable minimum in the penalty function, and no clear preference for fast-axis orientation within these cases (Figure 18).

Finally, we estimated RFs and Ps splitting for two target depths, 60 and 80 km, at station LSA to allow for some ambiguity for the true Moho within the thickened Tibet crust. Neither target depth offered a persuasive estimate of crustal-average birefringence. Figure 19 shows the harmonic decomposition for LSA at 60-km target depth. Figure 20 shows estimates for Ps birefringence for the Ps converted phase near this target depth.

GSN_Station_ARU Anisotropy/Dip Unmodelled Target Depth 40 km constant constant **Back Azimuth Expansion Terms** Back Azimuth Expansion Terms $cos(\xi)$ cos(E) sin(ξ) sin(E) $cos(2\xi)$ cos(2ξ) sin(2E) sin(2ξ) -3 0 3 -3 0 3 -6 -6 Delay Time (sec) Delay Time (sec)

Figure 17. Harmonic terms of back azimuth ξ fit by least-squares in the frequency domain to receiver-functions estimated from 739 earthquakes, with magnitude M = 6.0 or more, recorded during 2010-2018 at GSN station ARU (Arti, Russia). The RF traces are migrated for a target depth of 40 km. Bootstrap uncertainties are indicated with green. Left panel: combinations of radial and transverse RF harmonics predicted by the first-order perturbations to Ps caused by 1-D anisotropic layering. The labels " $\cos(\xi)$ ", " $\sin(\xi)$ ", etc., refer to the back-azimuth dependence of the radial RF; the transverse RF is phase-shifted by 90° in ξ . The inferred Moho Ps conversion sits near 0-s delay time on the "constant" harmonic, and is accompanied by substantial one-sided pulses on the " $\cos(\xi)$ " and " $\sin(2\xi)$ " harmonics. A smaller two-sided pulse on the " $\cos(2\xi)$ " harmonic resembles the birefringence signal in Figure 2. Right panel: combinations of radial and transverse RF harmonics that are not predicted by 1-D anisotropy to first order. The labels " $\cos(\xi)$ ", " $\sin(\xi)$ ", etc., refer to the back-azimuth dependence of the radial RF; the transverse RF is phase-shifted by -90° in ξ .

Ps Splitting for GSN Station ARU

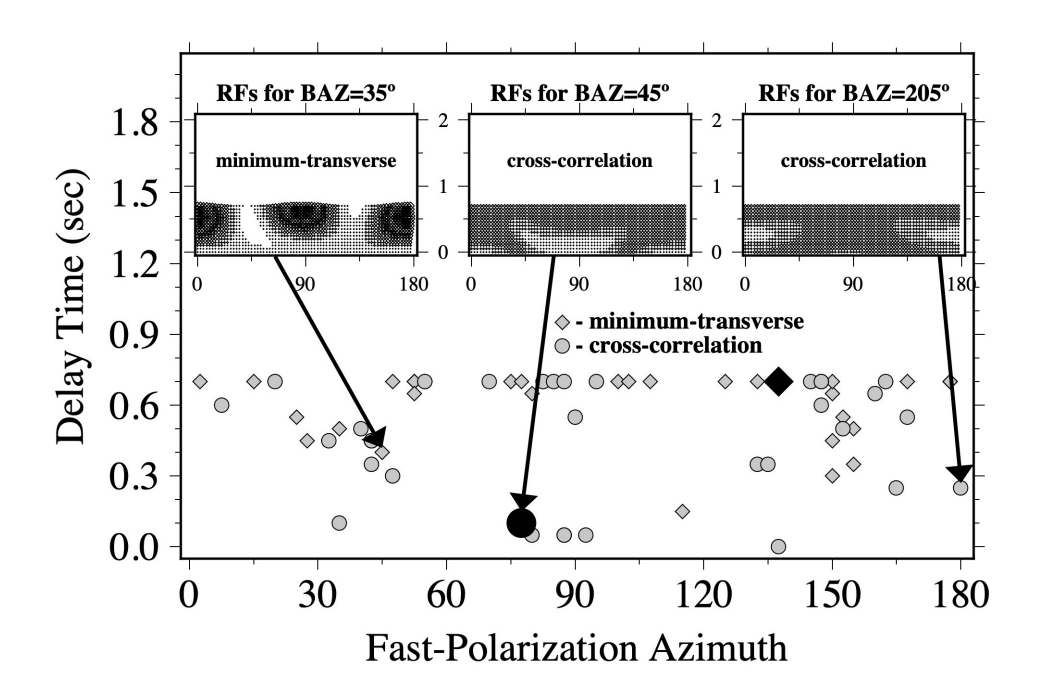


Figure 18. Ps birefringence estimated from 739 earthquakes recorded during 2010-2018 at GSN station ARU (Arti, Russia). Seismograms were processed and plotted in a manner similar to Figure 4, but with 2-second data windows centered on the inferred Moho Ps phase, with splitting times restricted to $\delta t < 0.75$ s. Minima of the minimum-transverse penalty function are plotted as grey diamonds. Minima of the cross-correlation penalty function are plotted as grey circles. The black diamond is the minimum of the summed minimum-transverse penalty-function surfaces. The black circle is the minimum of the summed cross-correlation penalty-function surfaces. The splitting penalty surfaces for three different RF pairs are plotted as insets; all display distinct penalty-function minima whose fast polarizations φ disagree. Many apparent splitting times for the RFs sit at the maximum tested value ($\delta t = 0.7$ s), but splitting-parameter estimates with longer time windows do not clarify the birefringence. Best splitting times δt at the minima for the summed penalty functions lies near zero for the cross-correlation metric and near the maximum for the minimum-transverse metric. The inferred fast polarizations φ disperse widely.

GSN_Station_LSA

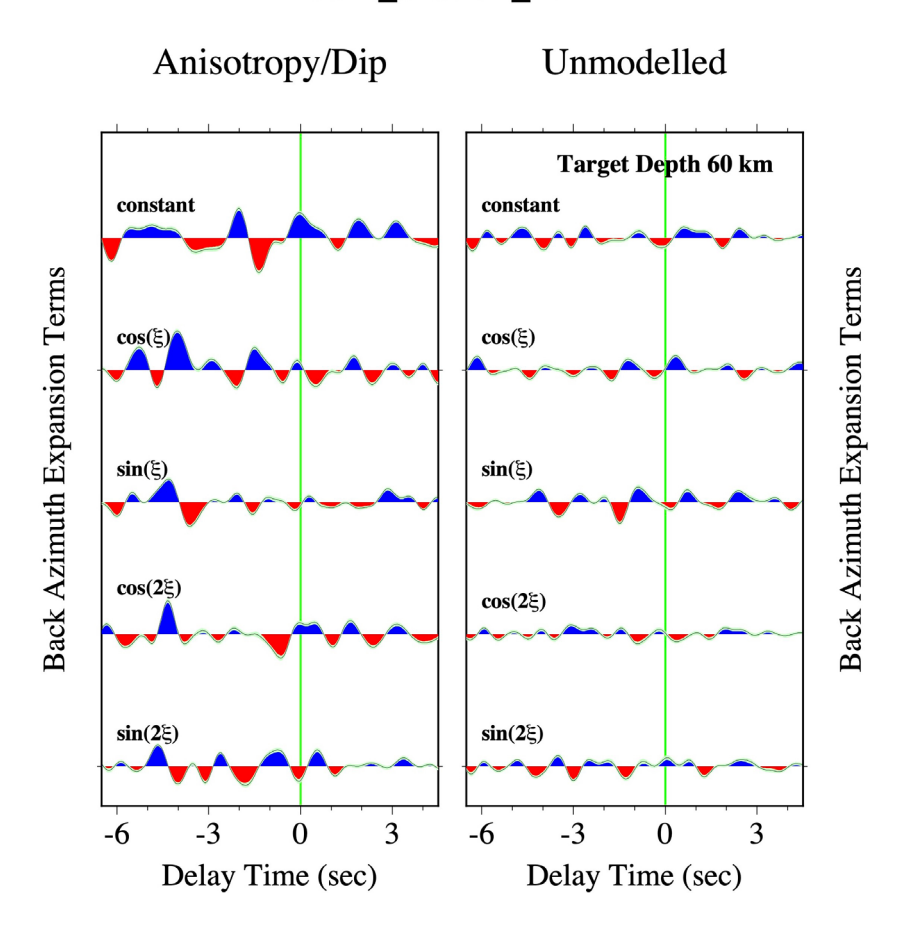


Figure 19. Harmonic terms of back azimuth ξ fit by least-squares in the frequency domain to receiver-functions estimated from 641 earthquakes, with magnitude M = 6.0 or more, recorded during 2014-2021 at GSN station LSA (Lhasa Tibet, China). The RF traces are migrated for a target depth of 60 km. Bootstrap uncertainties are indicated with green. Left panel: combinations of radial and transverse RF harmonics predicted by the first-order perturbations to Ps caused by 1-D anisotropic layering. The labels " $\cos(\xi)$ ", " $\sin(\xi)$ ", etc., refer to the back-azimuth dependence of the radial RF; the transverse RF is phase-shifted by 90° in ξ . The inferred Moho Ps conversion sits near 0-s delay time on the "constant" harmonic, and is accompanied by complex pulses on the " $\cos(2\xi)$ " and " $\sin(2\xi)$ " harmonics. Right panel: combinations of radial and transverse RF harmonics that are not predicted by 1-D anisotropy to first order. The labels " $\cos(\xi)$ ", " $\sin(\xi)$ ", etc., refer to the back-azimuth dependence of the radial RF; the transverse RF is phase-shifted by -90° in ξ .

Ps Splitting for GSN Station LSA

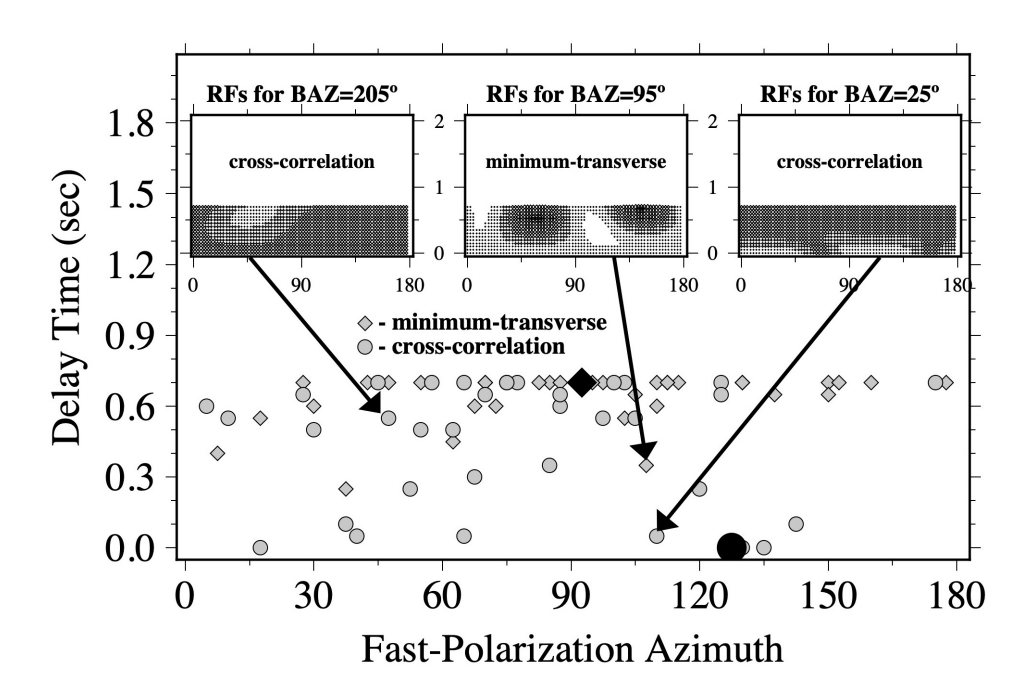


Figure 20. Ps birefringence estimated from 641 earthquakes recorded during 2014-2021 at GSN station LSA (Lhasa Tibet, China). Seismograms were processed and plotted in a manner similar to Figure 4, but with 2-second data windows centered on the inferred Moho Ps phase, with splitting times restricted to $\delta t < 0.75$ s. Minima of the minimum-transverse penalty function are plotted as grey diamonds. Minima of the cross-correlation penalty function are plotted as grey circles. The black diamond is the minimum of the summed minimum-transverse penalty-function surfaces. The black circle is the minimum of the summed cross-correlation penalty-function surfaces. The splitting penalty surfaces for three different RF pairs are plotted as insets; all display distinct penalty-function minima whose locations disagree. Many apparent splitting times for the RFs sit at the maximum tested value ($\delta t = 0.7$ s), but splitting-parameter estimates with longer time windows do not clarify the birefringence. Best splitting times δt at the minima for the summed penalty functions lies near zero for the cross-correlation metric and near the maximum for the minimum-transverse metric. The inferred fast polarizations ϕ disperse widely.

8. Discussion

The complications induced by plausible anisotropic layering and the failure of three seismic stations to exhibit a clear Ps birefringence signal does not invalidate the Ps-splitting technique, but should spark concerns. The use of Ps splitting as a tectonic probe, clearly, has limitations. Synthetic seismogram experiments find that birefringence estimates for the Moho Ps phase are reliable indicators of average-crust shear anisotropy only for cases where compressional anisotropy does not influence P-to-S conversion in the lower crust. Compressional anisotropy, especially for a tilted symmetry axis, induces harmonic Ps amplitude variations that interfere with similar variations induced by birefringence. In experiments with splitting estimates made from receiver functions, Moho Ps splitting that is influenced by deep-crustal compressional anisotropy (nonzero Backus parameter B) is scrambled together with other wave-propagation effects. For these cases wave-propagation calculations predict that estimates of Ps splitting span a wide range of possible fast-polarizations φ and that splitting times δ t can be determined by the thickness of lower-crust layers, not the average shear anisotropy. A researcher could easily mis-interpret a handful of internally-consistent Ps-splitting measurements from a narrow, but well-populated, back-azimuth sector, or misread a signal by discarding all complex waveforms in favor of a small number of fortuitously simple waveforms. The key point is that the effects of tilted symmetry axes and P-wave anisotropy are not random noise that will automatically disappear in a multi-event average. These waveform effects cause systematic bias.

Additional bias is predicted by our simulations with the oft-neglected Backus parameter C. Brownlee et al. [2017] reports that this $\cos 4\xi$ wavespeed variation tends to modify slightly the elliptical back-azimuthal wavespeed dependence of most crustal rocks. However the effects of C on P-to-S scattering amplitudes are larger, and we find cases where the 4-lobed signature of Ps splitting is displaced from Moho-Ps delay times to earlier times, which would confuse a birefringence estimate.

Early use of Ps-splitting times to separate the crustal anisotropic signal from a larger mantle signal involved analysis of isolated-event waveforms. Modern estimates are typically made from radial and transverse receiver functions estimated from large data sets, as with the RF analyses in this paper. The portions of these data sets suitable for birefringence estimates are often reported to be small fractions of otherwise adequate waveforms. Chen et al. [2013] isolated 647 splitting estimates from RFs from 7423 event-station pairs, fewer than 10 estimates per station on average. Xu et al. [2018] averages all RFs from 50-100 km station clusters within a dense network in Tibet, and plot RFs that show scarce internal structure within the thickened crust. Lack of anisotropic layering might benefit the estimates of Xu et al. [2018] but internal crustal structure is not discussed. On the other hand, Liu et al. [2015] and Xie et al. [2020] reported strong anisotropic layering within the crust from RFs estimated from single stations in the same sector of Tibet.

Some researchers have not estimated Ps birefringence directly. Kong et al. [2016] estimated crustal anisotropy in Tibet from radial-only receiver functions with sinusoidal back-azimuth variation in Ps delay times at 71 stations. They report discarding RFs with large coda signals, but do not report the proportion of seismic records that were discarded. Further investigation is needed to evaluate the robustness in a traveltime-only estimator for crustal anisotropy, though anisotropic scenarios that are similar to those shown for synthetic RFs in Figures 7, 8, and 12 would plausibly bias the estimator employed by Kong et al. [2016]. Note that the tight lowpass ($f_c = 0.8 \text{ Hz}$) employed by Kong et al. [2016] would meld together any Ps converted phases from interfaces less than 10 km from the Moho.

Finally, Nagaya et al. [2011] discount the effects of P-wave anisotropy with synthetic seismograms. Their synthetic waveforms, however, do not show 2-lobed Ps amplitude variation, despite their prescription of a 40° tilt in the lower-crust symmetry axis. Because both our own reflectivity synthetic seismograms [Levin and Park, 1997; Chen et al., 2021b], theoretical calculations from perturbation theory [Park and Levin, 2016a] and observational studies [Liu and Park, 2017; Xie et al., 2020] find abundant 2-lobed Ps amplitude variation, we are concerned about this Nagaya et al. [2011] interpretation. Rümpker et al. [2014] discuss the possible effects of anisotropic layering on Ps splitting, but do not discuss any biases associated with compressional anisotropy. Discounting P-wave anisotropy in their synthetic-seismogram Ps-splitting estimates is easier, though, because Rümpker et al. [2014] only considers anisotropic models with a horizontal axis of symmetry.

9. Conclusions

The birefringence of P-to-S converted waves from the Moho discontinuity is a reliable tool to constrain the anisotropy of Earth's crust only under restricted circumstances. The usual model for splitting involves shear anisotropy with a horizontal axis of symmetry, so that the splitting time is interpreted as a vertical average of anisotropy between the scattering point and the free surface. In addition to shear-wave birefringence, however, anisotropy has a substantial influence on the initial amplitude of the Ps converted wave, largely through the influence of compressional anisotropy, which is particularly efficient at altering Ps amplitudes if the symmetry axis is tilted. Compressional anisotropy is roughly comparable to shear anisotropy in most rocks [Ji et al., 2015], and deviations from a horizontal symmetry axis are common in Earth's crust [Levin and Park, 1997; Liu et al., 2015; Park and Rye, 2019; Xie et al., 2020]. Both these effects will disrupt the splitting signal acquired during the propagation of Ps from its scattering depth to the seismometer. We recognize these problematic behaviors in Ps-splitting analysis from three long-running permanent seismic stations. The scope of our data analysis is too narrow to discount Ps splitting as a general rule, and mainly serves as proof of the concepts suggested by the synthetic modelling. However, we believe that Ps birefringence is a problematic seismic observable and requires careful validation in any region with a complex tectonic history where crustal deformation is extensive.

The extension of our anisotropic models to the higher-order anisotropic Backus parameter C leads to significant, but not dramatic, changes in receiver-function amplitudes. These disruptions are greater than the modest deviations from ellipsoidal wavespeed variation predicted as a function of the angle ζ from the symmetry axis [Brownlee

et al., 2017]. For a dipping axis of symmetry, however, synthetic seismograms suggest that C induces significant perturbations to Ps amplitude that are constant with back azimuth ξ , with either positive or negative amplitudes. This behavior is much larger than constant- ξ perturbations from the low-order anisotropic Backus parameters B and E, and deserves attention as a possible trade-off with a crustal low-velocity layer.

Acknowledgements. We would like to thank Lucia Margheriti for inviting us to submit this paper to the special issue on shear-wave splitting. Two anonymous reviewers made useful comments on an earlier version of this paper, which hopefully improved in revision. The GSN is a cooperative scientific facility operated jointly by the National Science Foundation (NSF) and the United States Geological Survey (USGS), see SIO [1986] and ASL [1988; 1992]. The NSF component is part of NSF's SAGE facility, operated by the Incorporated Research Institutions for Seismology (IRIS) under Cooperative Support Agreement EAR-1851048. The figures were constructed using Generic Mapping Tools (Wessel and Smith, 1991). The RF timeseries were computed using anirec_synth code package and analyzed with rfmig_mcboot package (https://drive.google.com/drive/folders/0B5cfVtTS8QXZTGc1WnViSE5RWjA?resourcekey=0-YidcAd0wJGPR R1PhAyUYNA&usp=sharing). All seismic data were downloaded through IRIS Web Services (https://service.iris.edu/). Data were processed with Jupyter Notebooks developed by JP using the ObsPy package [Krischer et al., 2015]. JP was supported at Yale by U.S. NSF EAR-1818792, and XC and VL at Rutgers with NSF Grant EAR-1147831 and support from the Rutgers School of Graduate Studies for Xiaoran Chen.

References

- Albuquerque Seismological Laboratory (ASL)/USGS (1988). Global Seismograph Network (GSN IRIS/USGS). International Federation of Digital Seismograph Networks, doi:10.7914/SN/IU.
- Albuquerque Seismological Laboratory (ASL)/USGS (1992). New China Digital Seismograph Network. (GSN IRIS/USGS). International Federation of Digital Seismograph Networks, doi:10.7914/SN/IC.
- Backus, G. E. (1965). Possible forms of seismic anisotropy of the uppermost mantle under oceans. J. Geophys. Res., 70, 3429-3439.
- Barruol, G. and D. Mainprice (1993). A quantitative evaluation of the contribution of crustal rocks to the shear-wave splitting of teleseismic SKS waves, Phys. Earth Planet. Int., 78, 281-200.
- Bernard, R. E. and W. M. Behr (2017). Fabric heterogeneity in the Mojave lower crust and lithospheric mantle in Southern California, J. Geophys. Res., 122, 5000-5025.
- Bianchi, I., J. Park, N. P. Agostinetti and V. Levin (2010). Mapping seismic anisotropy using harmonic decomposition of receiver functions: an application to Northern Apennines, Italy, J. Geophys. Res., 115, B12317.
- Bowman, J. R. and M. Ando (1987). Shear-wave splitting in the upper mantle above the Tonga subduction zone, Geophys. J. Roy. Astron. Soc., 88, 25-41.
- Brownlee, S. J., V. Schulte-Pelkum, A. Raju, K. Mahan, C. Condit and O. F. Orlandini (2017). Characteristics of deep crustal seismic anisotropy from a compilation of rock elasticity tensors and their expression in receiver functions, Tectonics, 36, 1835-1857.
- Butler, R., T. Lay, K. Creager, P. Earle, K. Fischer, J. Gaherty, G. Laske, W. Leith, J. Park, M. Ritzwoller, J. Tromp and L. Wen (2004). The Global Seismographic Network surpasses its design goal, EOS Trans. AGU, 85, 225-229.
- Chen, X. (1993). A systematic and efficient method of computing normal modes for multilayered half-space. Geophys. J. Int., 115, 391-409.
- Chen, X., V. Levin, H. Yuan, M. Klaser and Y. Li (2021a). Seismic anisotropic layering in the Yilgarn and Superior cratonic lithosphere. J. Geophys. Res., 126, e2020JB021575.
- Chen, X., J. Park and V. Levin (2021b). Anisotropic layering and seismic body waves: Deformation gradients, initial S-polarizations, and converted-wave birefringence, Pure Appl. Geophys., 178, 2001-2023.
- Chen, Y., Z. Zhang, C. Sun and J. Badal (2013). Crustal anisotropy from Moho converted Ps wave splitting analysis and geodynamic implications beneath the eastern margin of Tibet and surrounding regions, Gondwana Research, 24, 946-957.
- Eckhardt, C. and W. Rabbel (2011). P-receiver functions of anisotropic continental crust: a hierarchic catalogue of crustal models and azimuthal waveform patterns, Geophys. J. Int., 187, 439-479.

- Ji, S., T. Shao, K. Michibayashi, S. Oya, T. Satsukawa, Q. Wang, W. Zhao and M. H. Salisbury (2015). Magnitude and symmetry of seismic anisotropy in mica- and amphibole-bearing metamorphic rocks and implications for tectonic interpretation of seismic data from the southeast Tibetan Plateau, J. Geophys. Res., 120, 6404-6430.
- Kong, F., J. Wu, K. H. Liu and S. S. Gao (2016). Crustal anisotropy and ductile flow beneath the eastern Tibetan Plateau and adjacent areas, Earth Planet. Sci. Letts., 442, 72-79.
- Krischer, L., T. Megies, R. Barsch, M. Beyreuther, T. Lecocq, C. Caudron and J. Wassermann (2015). ObsPy: A bridge for seismology into the scientific Python ecosystem, Comput. Sci. & Discovery, 8, 014003.
- Levin, V., L. Margheriti, J. Park and A. Amato (2002). Anisotropic seismic structure of the lithosphere beneath the Adriatic coast of Italy constrained with mode-converted body waves, Geophys. Res. Letts., 29, 2058.
- Levin, V., W. Menke and J. Park (1999). Shear-wave splitting in Appalachians and Urals: A case for multilayered anisotropy, J. Geophys. Res., 104, 17975-17994.
- Levin, V. and J. Park (1997). P-SH conversions in a flat-layered medium with anisotropy of arbitrary orientation. Geophys. J. Int., 131, 253-266.
- Levin, V. and J. Park (1998). P-SH conversions in layered media with hexagonally symmetric anisotropy: A cookbook, Pure Appl. Geophys., 151, 669-697.
- Levin, V. and J. Park (2000). Shear zones in the Proterozoic lithosphere of the Arabian Shield and the nature of the Hales discontinuity, Tectonophysics, 323, 131-148.
- Li, Y., V. Levin, A. Nikulin and X. Chen (2021). Systematic mapping of upper mantle seismic discontinuities beneath northeastern North America. Geochem. Geophys. Geosys., 22, e2021GC009710.
- Ligorria, J. P. and C. J. Ammon (1999). Iterative deconvolution and receiver-function estimation, Bull. Seismol. Soc. Am., 89, 1395-1400.
- Liu, Z., J. Park and D. M. Rye (2015). Crustal anisotropy in northeastern Tibetan Plateau inferred from receiver functions: rock textures caused by metamorphic fluids and lower crust flow? Tectonophysics, 661, 66-80.
- Liu, Z. and J. Park (2017). Seismic receiver function interpretation: Ps splitting or anisotropic underplating?, Geophys. J. Int., 208, 1332-1341.
- Maupin, V. and J. Park (2015). Theory and Observations Seismic Anisotropy. In: Treatise on Geophysics, 2nd edition, Volume 1, Gerald Schubert (Editor-in-chief), Oxford, Elsevier, 277-305.
- McNamara, D. E. and T. J. Owens (1993). Azimuthal shear wave velocity anisotropy in the Basin and Range Province using Moho Ps converted phases, J. Geophys. Res., 98, 12003-12017.
- McNamara, D. E., T. J. Owens, P. G. Silver and F. T. Wu (1994). Shear wave anisotropy beneath the Tibetan Plateau, J. Geophys. Res., 99, 13655-13665.
- Nagaya, M., H. Oda and T. Kamimoto (2011). Regional variation in shear-wave polarization anisotropy of the crust in southwest Japan as estimated by splitting analysis of Ps-converted waves on receiver functions, Phys. Earth Planet. Int., 187, 56-65.
- Nikulin, A., V. Levin and J. Park (2009). Receiver function study of the Cascadia megathrust: Evidence for localized serpentinization. Geochem. Geophys. Geosyst., 10, Q07004.
- Olugboji, T. M. and J. Park (2016). Crustal anisotropy beneath Pacific Ocean islands from harmonic decomposition of receiver functions, Geochem. Geophys. Geosyst., 17, 810-832.
- Park, J. (1996). Surface waves in layered anisotropic structures. Geophys. J. Int., 126, 173-183.
- Park, J. and V. Levin (2000). Receiver functions from multiple-taper spectral correlation estimates. Bull. Seismol. Soc. Am., 90, 1507-1520.
- Park, J. and V. Levin (2016a). Anisotropic shear zones revealed by back-azimuthal harmonics of teleseismic receiver functions, Geophys. J. Int., 207, 1216-1243.
- Park, J. and V. Levin (2016b). Statistics and frequency-domain moveout for multiple-taper receiver functions. Geophys. J. Int., 207, 512-527.
- Park, J. and D. M. Rye (2019). Why is crustal underplating beneath many hotspot islands anisotropic?, Geochem. Geophys. Geosyst., 20, doi:10.1029/2019GC008492.
- Park, J., H. Yuan and V. Levin (2004). Subduction-zone anisotropy under Corvallis, Oregon: A serpentinite skidmark of trench-parallel terrane migration?, J. Geophys. Res., 109, B10306.
- Porter, R., G. Zandt and N. McQuarrie (2011). Pervasive lower-crustal seismic anisotropy in Southern California: Evidence for underplated schists and active tectonics, Lithosphere, 3(3), 201-220.
- Raitt, R. W., G. G. Shor, T. J. G. Francis and G. B. Morris (1969). Anisotropy of the Pacific upper mantle, J. Geophys. Res., 74, 3095-3109.

- Rümpker, G., A. Kaviani and K. Latifi (2014). Ps-splitting analysis for multilayered anisotropic media by azimuthal stacking and layer stripping, Geophys. J. Int., 199, 146-163.
- Savage, M. K. (1998). Lower crustal anisotropy or dipping boundaries? Effects on receiver functions and a case study in New Zealand, J. Geophys. Res., 103, 15,069-15,087.
- Schulte-Pelkum, V. and K. H. Mahan (2014). A method for mapping crustal deformation and anisotropy with receiver functions and first results from USArray. Earth Planet. Sci. Letts., 402, 221-233.
- Scripps Institution of Oceanography (SIO) (1986). IRIS/IDA Seismic Network. International Federation of Digital Seismograph Networks. Dataset/Seismic Network, doi:10.7914/SN/II.
- Shiomi, K. and J. Park (2008). Structural features of the subducting slab beneath the Kii Peninsula, central Japan: Seismic evidence of slab segmentation, dehydration, and anisotropy, J. Geophys. Res., 113, B10318.
- Sileny, J. and J. Plomerova (1996). Inversion of shear-wave splitting parameters to retrieve three-dimensional orientation of anisotropy in continental lithosphere, Physics Earth Planet. Int., 95, 277-292.
- Silver, P. G. and W. W. Chan (1991). Shear wave splitting and subcontinental mantle deformation, J. Geophys. Res., 96, 16429-16454.
- Silver, P. G. and M. K. Savage (1994). The interpretation of shear-wave splitting parameters in the presence of two anisotropic layers, Geophys. J. Int., 119, 949-963.
- Tesoniero, A., K. Leng, M. D. Long and T. Nissen-Meyer (2020). Full wave sensitivity of SK(K)S phases to arbitrary anisotropy in the upper and lower mantle, Geophys. J. Int., 222, 412-435.
- Vinnik, L. P. (1977). Detection of waves converted from P to SV in the mantle, Phys. Earth Planet. Int., 15, 39-45.
- Vinnik, L. P., G. L. Kosarev and L. I. Makeyeva (1986). Azimuthal anisotropy of the Earth's interior from observations of long-period body waves, Izvestia Earth Physics, 22, 955-960.
- Wessel, P. and W. H. F. Smith (1991). Free software helps map and display data, EOS, Trans. AGU, 72, 441-446.
- Wirth, E. A. and M. D. Long (2012). Multiple layers of seismic anisotropy and a low-velocity region in the mantle wedge beneath Japan: Evidence from teleseismic receiver functions, Geochem. Geophys. Geosyst., 13, Q08005.
- Wüstefeld, A., G. Bokelmann, C. Zaroli and G. Barruol (2008). SplitLab: A shear-wave splitting environment in Matlab, Comput. Geosci., 34, 515-528.
- Xie, Z., V. Levin and Q. Wu (2020). Crustal anisotropy beneath northeastern Tibetan Plateau from the harmonic decomposition of receiver functions, Geophys. J. Int., 220, 1585-1603.
- Xu, X., F. Niu, Z. Ding and Q. Chen (2018). Complicated crustal deformation beneath the NE margin of the Tibetan plateau and its adjacent areas revealed by multi-station receiver-function gathering, Earth Planet. Sci. Letts., 497, 204-216.